Chapter 9
A Self-assembled Quantum Dot as Single Photon Source and Spin Qubit: Charge Noise and Spin Noise

Richard J. Warburton

Abstract A self-assembled quantum dot confines both electrons and holes to a nano-sized region inside a semiconductor. An exciton in a single self-assembled quantum dot is a potentially excellent source of single photons. A quantum dot also acts as a host for a spin qubit with the advantage that the spin can be initialized, manipulated and read-out with optical techniques. However, the exciton and spins couple strongly not just to an external optical probe but also to internal excitations of the host semiconductor: the semiconductor is a source of noise resulting in exciton and spin dephasing. The noise can be suppressed in some cases, circumvented in others, leading to an improvement in quantum dot performance. In particular, resonant excitation at low temperature using high quality material results in a small level of charge noise. A heavy hole spin in an in-plane magnetic field is decoupled from the spin noise arising from fluctuations in the nuclear spin bath. Presented here is a series of experiments which probe the noise in advanced quantum dot devices: single quantum dot resonance fluorescence as a sensor of both charge noise and spin noise; nuclear magnetic resonance on the quantum dot nuclear spins to probe the electron spin hyperfine interaction; and coherent population trapping to probe the hole spin hyperfine interaction.

9.1 A Self-assembled Quantum Dot for Quantum Technology

A self-assembled quantum dot in GaAs has a nano-size, typically 20 nm in base diameter, 5 nm in height, resulting in discrete, atom-like quantum states. This small size, a size which is difficult to access with top-down nano-fabrication, confers an immediate advantage: both the confinement energies and on-site Coulomb interactions are large, tens of meV. The net result is that Coulomb blockade is well established: ultra-low temperatures are not required. Also, the self-assembly process along with

R.J. Warburton (✉)
Department of Physics, University of Basel,
Klingelbergstrasse 82, 4056 Basel, Switzerland
e-mail: richard.warburton@unibas.ch

P. Michler (ed.), *Quantum Dots for Quantum Information Technologies*,
Nano-Optics and Nanophotonics, DOI 10.1007/978-3-319-56378-7_9

the direct gap of the host semiconductor results in a strong optical transition across the fundamental gap of the semiconductor: the optical dipole moment is large. This, together with the large number of photon modes in a bulk structure, leads to short radiative lifetimes, ∼0.8 ns.

A self-assembled quantum dot is potentially useful in quantum technology, as a single photon source and as a spin qubit. On the one hand, self-assembled quantum dots can be embedded in semiconductor heterostructures, and devices can be made from the wafer material by semiconductor nano-fabrication for which a large and established tool-box is available. On the other hand, electrons and holes in the quantum dot are not just strongly coupled to external probes such as the light field: they are also strongly coupled to excitations in the host semiconductor. This means that dephasing, the interaction of quantum dot-based quantum states with the semiconductor environment, is strong and it is challenging to design structures where the dephasing is kept to a manageable level. In fact much of the interesting physics lies in the dephasing which can be complex [1].

This chapter describes a series of experiments on single self-assembled quantum dots. The aim of these experiments is to investigate the noise which limits the performance of the quantum dot as a single photon emitter and as a spin qubit. An underlying feature is the use of high quality material at low temperature, and resonant optical excitation with resonance fluorescence detection.

9.2 Photonics of a Self-assembled Quantum Dot

9.2.1 The Optical Transition

An InGaAs/GaAs quantum dot, Fig. 9.1a, has a strong optical transition between the highest valence state and the lowest conduction state [2]. In semiconductor language, optical excitation creates an exciton, an electron-hole pair. For as-grown InAs/GaAs quantum dots, the optical transition lies at an inconvenient wavelength, ∼1,200 nm at low temperature, but can be shifted to the more convenient ∼950 nm either during growth [3] or via post-growth annealing [4]. The radiative lifetime is short, typically ∼0.8 ns [5], corresponding to a dipole moment of 0.6e nm·C [6]. The level structure is explained in Fig. 9.1b–d. Note that the two bright excitons with spin ± 1 are coupled by the so-called fine structure: this lifts the degeneracy of the two exciton states even at zero magnetic field.

The main optical transition forms the basis of a quantum dot single photon source. The problem of extracting the photons out of the high-index host material – GaAs has a refractive index of 3.5 – can be solved by engineering also the photonic states. For instance, by embedding the quantum dots in a GaAs waveguide, and using a taper as an out-coupler, high fidelity single photon emission with a quantum efficiency as high as ∼70% has been achieved [7].

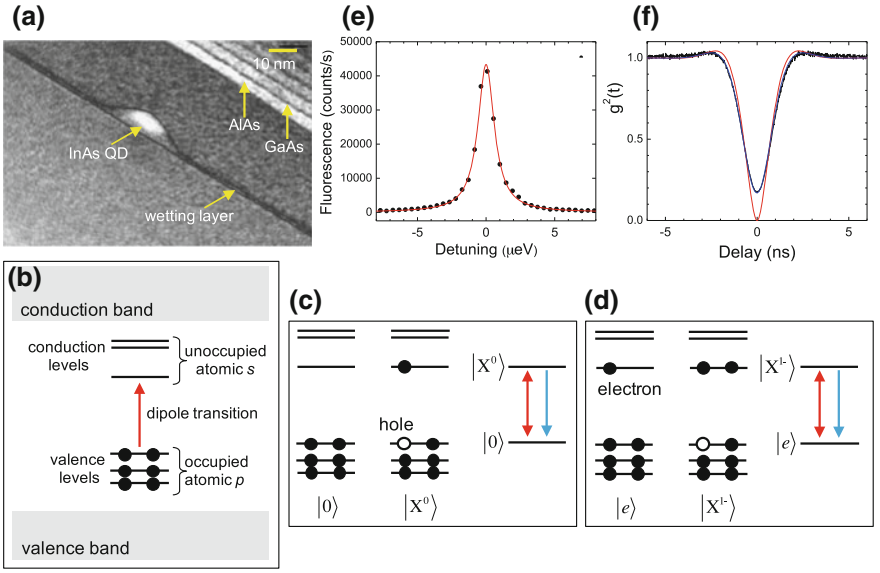

Fig. 9.1 Photonics of a single self-assembled quantum dot at zero magnetic field. **a** Transmission electron microscopy image of a sample grown by molecular-beam-epitaxy showing an InAs quantum dot with its associated wetting layer, embedded in GaAs and capped with an AlAs/GaAs superlattice. Image provided courtesy of Jean-Michel Chauveau, Arne Ludwig, Dirk Reuter and Andreas Wieck. **b** Schematic energy level structure of a self-assembled quantum dot. On account of quantization, there are discrete, atom-like conduction and valence levels with wave functions localized in the quantum dot. At higher energies, there are the conduction and valence energy bands associated with the two-dimensional wetting layer (and bulk GaAs at higher energy still). At low temperature and in the absence of doping, the valence levels are occupied and the conduction levels are unoccupied. A strong optical dipole transition connects the highest energy valence level with the lowest energy conduction level, the transition taking place across the fundamental gap of the semiconductor. **c** The vacuum state $|0\rangle$ and the optically excited state $|X^0\rangle$ are represented as the ground and excited states of a 2-level atom (*red arrow* represents the optical coupling, *blue arrow* spontaneous emission). In $|X^0\rangle$, a valence electron has been promoted to a conduction level creating a so-called exciton, an electron-hole pair. **d** A quantum dot can be loaded with a single excess electron (see Fig. 9.2). In this case, the ground state is $|e\rangle$ and the optically excited state $|X^{1-}\rangle$ consisting of two electrons (in a singlet) and a hole. **e** Laser spectroscopy on a single quantum dot at a wavelength close to 950 nm at temperature 4.2 K. The resonance fluorescence is plotted as a function of laser detuning. The linewidth is 1.6 μeV (400 MHz). The signal corresponds to the count rate on a silicon avalanche photodiode. The transform-limited linewidth is $\Gamma_0 = 0.8$ μeV, equivalently 200 MHz (radiative lifetime 0.8 ns). **f** The intensity correlation coefficient $g^{(2)}$ of the resonance fluorescence measured with a Hanbury Brown-Twiss interferometer (*black line*). The dip at zero delay shows clear photon antibunching. The signal at zero delay is dominated by the jitter of the detector (0.5 ns); the slight overshoot at delay ∼1 ns is the first hint of a Rabi oscillation which becomes marked at higher laser power. The *blue line* is a convolution of the two-level atom $g^{(2)}$ with the response of the detectors; the *red line* is the two-level atom $g^{(2)}$ alone. **e**, **f** data courtesy of Andreas Kuhlmann, Julien Houel and Arne Ludwig

9.2.2 Vertical Tunneling Structures

Implementing the concept of an electron spin qubit [8] with a self-assembled quantum dot involves trapping a single electron. This can be achieved by including a δ-doped layer close to the quantum dot layer in the growth such that some of the quantum dots are permanently occupied with an excess electron [9] or hole [10] at low temperature. A more flexible technique allowing for considerable in situ tuning is to embed the quantum dot layer in a vertical tunnelling device [2, 11, 12], Fig. 9.2a. The device operates in the Coulomb blockade regime which at 4 K is highly pronounced based on the huge on-site Coulomb energy to thermal energy ratio ($\sim$25 meV : 0.4 meV). The quantum dots are in tunnel contact with a Fermi sea; the quantum dot potential with respect to the Fermi energy is controlled by applying a gate voltage to the top contact. The top contact is often a Schottky gate on the sample surface, an n-i-Schottky structure with the quantum dots in the intrinsic "i" region. Alternatively, the Schottky contact can be replaced with a p-type layer, an n-i-p structure where the p-type layer acts as an "epitaxial gate" [13].

Structures for trapping a single hole swap n-doping for p-doping, i.e. p-i-Schottky and p-i-n. However, quantum dots grown after the p-type layer have relatively poor optical properties [13, 15]. The solution is the n-i-p structure with the quantum dots in tunnel contact with the p-layer as in this case the p-type layer is grown last, Fig. 9.3.

In these structures, the Coulomb blockade is revealed most immediately in the single quantum dot photoluminescence by clear steps in the photoluminescence energy [12], Fig. 9.2b. A single electron is trapped in the quantum dot over the Coulomb blockade plateau, Fig. 9.2b: a voltage chosen within this region allows access to single spin physics [16]. In the Coulomb blockade regime, tunnelling is suppressed to first order but the second order process, co-tunnelling, survives [17]. Co-tunnelling represents a spin relaxation mechanism: the quantum dot electron spin is swapped by a two-electron process with the spin of an electron close to the Fermi energy in the Fermi sea of the n^+ layer. A convenient property of the vertical tunnelling structure is that the co-tunnelling rate is large at the edge of the plateau but is suppressed by several orders of magnitude in the plateau centre, providing useful in situ control [17–21].

The tunnel barrier thickness is important. For very small values, the quantum states hybridize strongly with the states at the Fermi energy in the back contact [22]; at very large values, the tunneling time becomes much longer than the recombination time. An important point of detail in these structures concerns the thickness of the capping layer, the i-GaAs grown between the quantum dot layer and the blocking barrier (an AlAs/GaAs superlattice). At intermediate thicknesses, fluctuating minority carriers at the GaAs/blocking barrier interface result in unwanted charge noise [23]. This noise can be suppressed with a thin $\sim$10 nm capping layer pushing the minority charge states well above the quantum dot levels such that the states are unlikely to be occupied at low temperature. A thin capping layer also prevents the optically-excited minority carrier (the hole in the case of an electron spin device; the electron in the case of a hole spin device) from tunneling out of the quantum dot.

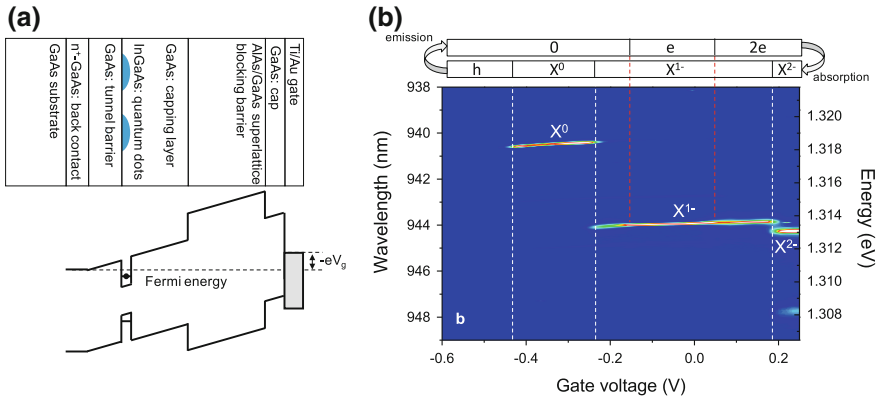

Fig. 9.2 Coulomb blockade of a single quantum dot. **a** Layer structure of a typical heterostructure for experiments controlling the charge state of a quantum dot. A layer of self-assembled quantum dots is embedded in a vertical tunnelling structure. The quantum dots are in tunnel contact with the Fermi sea in the n^+ layer; the blocking barrier prevents current flow to the surface; a Schottky gate on the surface allows control of the vertical electric field. Typically, the tunnel barrier (gallium arsenide, GaAs) is 12–40 nm thick, the capping layer 10–150 nm, blocking barrier > 100 nm, and the Schottky gate is a semi-transparent metal layer, e.g. 5–10 nm Ti/Au. A voltage applied to the gate, V_g, tunes the energy of the first confined electron level relative to the Fermi energy as shown schematically in the band diagram. At low temperature and large electric field, the quantum dot conduction level lies above the Fermi energy and is therefore unoccupied; when the conduction level lies below the Fermi energy but close to it (the case shown), the conduction level is singly occupied (the case shown); at more positive V_g it is doubly occupied. **b** The photoluminescence (PL) from a single quantum dot in a vertical tunnelling structure is shown as a function of V_g at a temperature of 4.2 K. The steps in the photoluminescence energy correspond to charging events. X^0 refers to the neutral exciton (an electron-hole pair); X^{1-} to the negatively charged trion (a two electron-one hole complex); X^{2-} the doubly charged exciton (a three electron-one hole complex). Note that the charging event without a hole, $|0\rangle \rightarrow |e\rangle$, takes place at slightly more positive V_g than the charging event with a hole, $|X^0\rangle \rightarrow |X^{1-}\rangle$, on account of the Coulomb energies: the electron-hole on-site Coulomb energy is larger than the electron-electron on-site Coulomb energy. Conversely, the $|e\rangle \rightarrow |2e\rangle$ charging event takes place at more negative V_g than the $|X^{1-}\rangle \rightarrow |X^{2-}\rangle$ charging event as the $|X^{2-}\rangle$ state has a total of three electrons, the "third" forced to occupy the first excited conduction level by the Pauli principle. The main features in the PL characterization correspond to charging events in the initial state, the exciton state (*white dashed lines*). However, charging events in the final state are revealed by hybridization effects in the X^{1-} plateau (*red dashed lines*) [14]. Probing a single spin with resonant laser excitation involves working in the V_g window defined by the two dashed red lines. Experimental data provided courtesy of Paul Dalgarno

9.2.3 Resonance Fluorescence Detection

Many optical experiments in this field rely on non-resonant excitation in which a high-energy continuum is occupied with electron-hole pairs. The exciton level in the quantum dot is populated by typically fast relaxation, and the spontaneous emission on exciton decay (the photoluminescence) can be detected. An example is shown in Fig. 9.2b. This is a relatively simple experiment but lacks the power of true laser

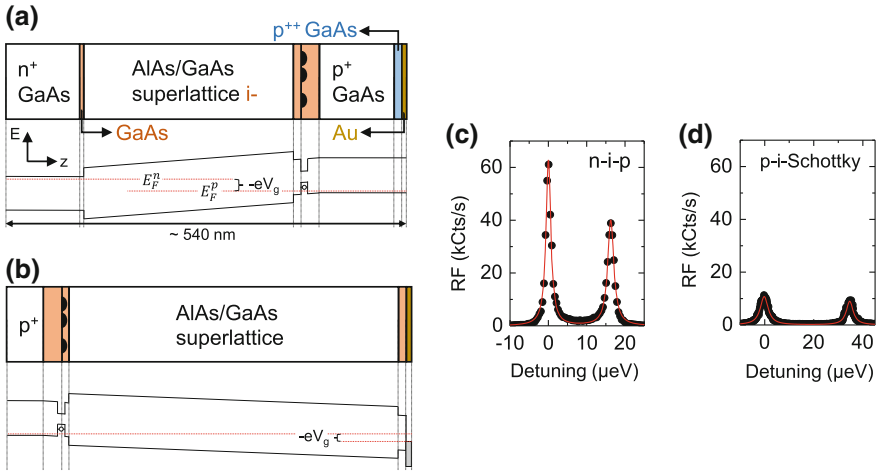

Fig. 9.3 Devices for loading a quantum dot with a single hole. **a** n-i-p device; **b** p-i-Schottky device: heterostructure design and schematic band diagram. **c** Resonance fluorescence spectrum at 4.2 K on an empty quantum dot in the p-i-n device. The two lines (split by the exciton fine structure) have a linewidth of 1.5 μeV, equal to the linewidth in the very best n-type devices, demonstrating the extremely low level of charge noise. **d** Resonance fluorescence spectrum at 4.2 K on an empty quantum dot in the p-i-Schottky device. The larger linewidths of 3.6 μeV and also the smaller signals signify problems related to the p-doping: increased charge noise and non-radiative decay

spectroscopy methods which involve driving the optical resonance with a coherent laser. The interaction of a single self-assembled quantum dot with a coherent laser tuned to the optical resonance was initially detected via a change in the transmission coefficient, a "ΔT-experiment" [24]. Meanwhile, the resonance fluorescence can also be detected (see also Chap. 3), discriminating resonance fluorescence from scattered/reflected laser light with a dark field technique based either on the propagation direction [25] or on the polarization [26–29], Fig. 9.1e. Remarkably, all the features of a driven two-level system known from atomic physics have been observed on a single quantum dot. These include a Lorentzian absorption lineshape [24], Fig. 9.1e; power broadening and power-induced transparency [30]; the ac Stark effect [31]; Rabi oscillations [25], the Mollow triplet, and antibunching of resonance fluorescence [25], Fig. 9.1f. Routinely, close-to-transform limited optical transitions are observed in laser spectroscopy experiments on single InGaAs/GaAs quantum dots [23]. Phonon-induced exciton decoherence is significant either at low temperature with large Rabi couplings [32, 33], or at elevated temperatures [30, 34–36].

The capability to detect resonance fluorescence has given the field a significant boost: the resonance fluorescence itself represents single photon output; in spectroscopy terms it is a low noise, low background technique.

9.3 Exciton Dephasing

A key goal in quantum communication is to create highly indistinguishable photons which are separated in space by more than 100 Km for device-independent quantum key distribution and for a quantum repeater [37]. This is potentially possible using a semiconductor quantum dot: single photons are generated either by spontaneous emission from the upper level [38–40], Fig. 9.1, or by coherent scattering of a resonant laser [41–43]. Optimizing performance demands an understanding of noise and a strategy to circumvent its deleterious effects [1]. There are two main sources of noise in a semiconductor. Charge noise arises from occupation fluctuations of the available states and leads to fluctuations in the local electric field. This results in shifts in the optical transition energy of a quantum dot via the dc Stark effect and is one mechanism by which the optical linewidth of a self-assembled quantum dot can be significantly increased above the transform limit [18, 23, 24]. Charge noise can also result in spin dephasing via the spin-orbit interaction, and, in particular for hole spins, via the electric field dependence of the g-factor [44, 45]. The second source of noise, spin noise, arises typically from fluctuations in the nuclear spins of the host material and, on account of the hyperfine interaction, results in a fluctuating magnetic field (the Overhauser field) experienced by an electron spin [46, 47]. Spin noise from noisy nuclei results in rapid spin dephasing in an InGaAs quantum dot [9, 48, 49].

Strategies for reducing noise involve working with ultra-clean materials to minimize charge noise and the use of dynamic decoupling, schemes which employ complex echo-like sequences to "protect" the qubit from environmental fluctuations [50–52]. In this case, it is absolutely crucial that the noise power decreases with increasing frequency.

For quantum dot-based single photon sources, the linewidths are in the best case (high quality material with resonant excitation) typically about a factor of two larger than the transform limit in which the linewidth is determined only by the radiative decay time [18, 23, 24], Fig. 9.1. This is a poor state of affairs for applications which rely on photon indistinguishability, the resource underpinning a quantum repeater for instance. On the positive side, there is evidence that with low power, resonant excitation, there is no significant upper level dephasing apart from radiative recombination [41, 42] such that over short timescales indistinguishable photons are emitted [39]. It has been surmised that the increase in linewidth above the ideal limit arises from a spectral wandering [23, 24].

The particular challenge posed by charge noise in self-assembled quantum dot devices is illustrated in Fig. 9.4. In this experiment, resonant laser spectroscopy on single quantum dots was carried out as a function of the power of an additional non-resonant laser [23]. The non-resonant laser is weak such that the induced photoluminescence is negligible but it introduces a small number of holes in the device. A steady state population of holes builds up at the capping layer/blocking barrier interface, in this case 35 nm above the quantum dot layer. The quantum dot transition frequency increases step-wise, Fig. 9.4. The interpretation is that there are localiza-

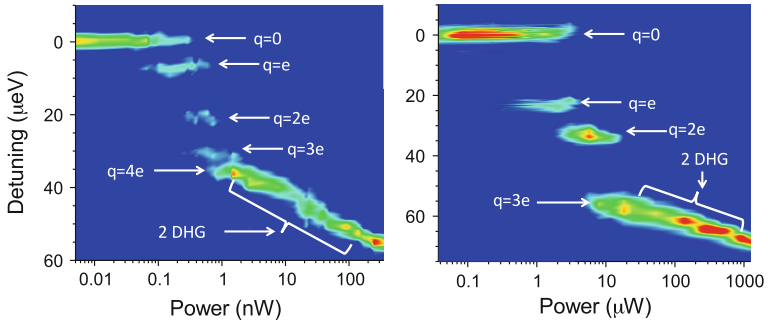

Fig. 9.4 Resonant laser spectroscopy on single quantum dots with close-by charge localization centres. Colour-scale plot (linear scale, *blue*: 0.061%; *red*: 0.61%) of differential reflectivity versus non-resonant laser power on two different quantum dots. The non-resonant laser power controls the steady state occupation of defects, hole localization centres located 30 nm above the quantum dot at the capping layer/blocking barrier interface. The charge is labelled in each case. At large non-resonant laser power, a two-dimensional hole gas forms (2DHG)

tion centres for the holes directly above the quantum dot. Occupation of one of these localization centres by a single hole shifts the quantum dot frequency by several linewidths, suppressing the resonance scattering. On the one hand, the sensitivity of the quantum dot to the small levels of charge noise reflects the potential of quantum dots as ultra-sensitive electrometers [23, 53, 54]. On the other hand, the same sensitivity makes the generation of transform-limited single photons challenging. The mechanism is the dc Stark effect [55].

9.3.1 The Charged Exciton

The resonance fluorescence signal itself can be used to investigate the noise [28, 56]. The linewidth determines the spectral purity of the single photons. Measured on second time-scales, the single quantum dot linewidths are 1.6 μeV in Fig. 9.5 for both neutral and charged excitons, X^0 and X^{1-}, respectively. The linewidth can be recorded on smaller time-scales: Fig. 9.5 shows the linewidths versus scanning frequency. The linewidths are constant up to about 1 kHz and then decrease, reaching constant values above about 50 kHz. Remarkably, the constant values at the highest frequencies correspond closely to the transform limit. (The difference in X^0 and X^{1-} transform-limited linewidths reflects the slightly different radiative decay times [5].) The implication is two-fold. First, any pure exciton dephasing mechanisms must be much weaker than radiative recombination in this experiment. Secondly, the quantum dot produces a stream of identical photons over time-scales of about 1–10 μs: over this time the noise is "frozen". At longer times, there are fluctuations in the quantum dot's optical frequency, a spectral wandering.

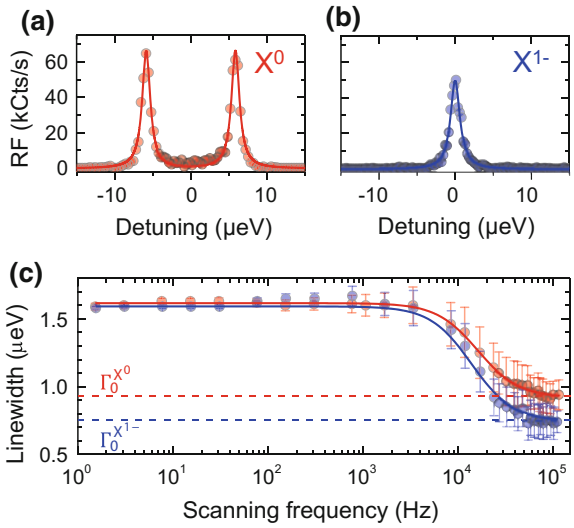

Fig. 9.5 Linewidth versus scanning frequency. **a**, **b** X^0, X^{1-} resonance fluorescence versus detuning δ at 4.2 K, $B = 0.0$ mT with 100 ms integration time per point. The *solid lines* are Lorentzian fits to the data. The linewidths are $\Gamma^{X^0} = 1.29\,\mu$eV, $\Gamma^{X^{1-}} = 1.49\,\mu$eV; the Rabi energies $\Omega/\Gamma_0 = 0.5$ (X^0), 0.4 (X^{1-}); and transform-limits $\Gamma_0^{X^0} = 0.92 \pm 0.10\,\mu$eV, $\Gamma_0^{X^{1-}} = 0.75 \pm 0.10\,\mu$eV. **c** RF linewidth against scanning frequency $d\delta/dt/\Gamma_0$. Γ approaches Γ_0 for scanning frequencies above 50 kHz. For each scanning frequency, the error bar represents the standard deviation of several hundred linewidth scans. *Solid lines* represent a Lorentzian fit of the data with linewidth 30 ± 3 kHz

An immediate question concerns the origin of the noise which leads to the spectral wanderings in the quantum dot's optical frequency. Insight comes from a noise spectrum of the resonance fluorescence: a time-trace is recorded at a particular detuning, $\delta = 0$ or $\delta = \Gamma/2$, Fig. 9.6a; a Fourier transform yields a noise spectrum [28, 56]. A typical time trace of the RF is shown in Fig. 9.6b with binning time 10 ms. The main contribution to the noise comes from shot noise. However, the level of extrinsic noise is highly reproducible: its spectrum, $N_{\mathrm{EXP}}(f)$, is recorded carefully and then subtracted from the total noise to determine the intrinsic noise, the noise power of the normalized RF signal, $N_{\mathrm{QD}}(f)$, Fig. 9.7a. Specifically, the fast Fourier transform (FFT) of the normalized RF signal $S(t)/\langle S(t)\rangle$ provides a noise spectrum:

$$N_{\mathrm{RF}}(f) = |\mathrm{FFT}[S(t)/\langle S(t)\rangle]|^2 (t_{\mathrm{bin}})^2/T, \tag{9.1}$$

where t_{bin} is the binning time and T the total integration time. $N_{\mathrm{QD}}(f)$ is determined by

$$N_{\mathrm{QD}}(f) = N_{\mathrm{RF}}(f) - N_{\mathrm{EXP}}(f). \tag{9.2}$$

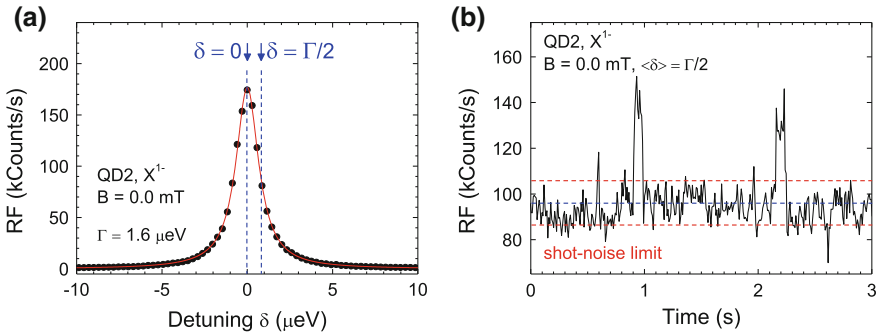

Fig. 9.6 Resonance fluorescence (RF) on a single quantum dot. **a** RF recorded on a single InGaAs quantum dot at wavelength 950.61 nm at a power corresponding to a Rabi energy of 0.55 μeV at a temperature of 4.2 K without external magnetic field. The RF was detected with a silicon avalanche photodiode operating in single photon mode; the detuning was achieved by sweeping the gate voltage with respect to the laser using the dc Stark effect. In this case, the integration time per point was 100 ms. The *solid line* is a Lorentzian fit to the data with linewidth $\Gamma = 1.6\,\mu$eV (390 MHz). **b** A time-trace of the RF recorded with detuning set to half the linewidth, $\langle\delta\rangle = \Gamma/2$. The arrival time of each detected photon is stored allowing a time trace to be constructed post-experiment with an arbitrary binning time. An example is shown using a binning time of 10 ms

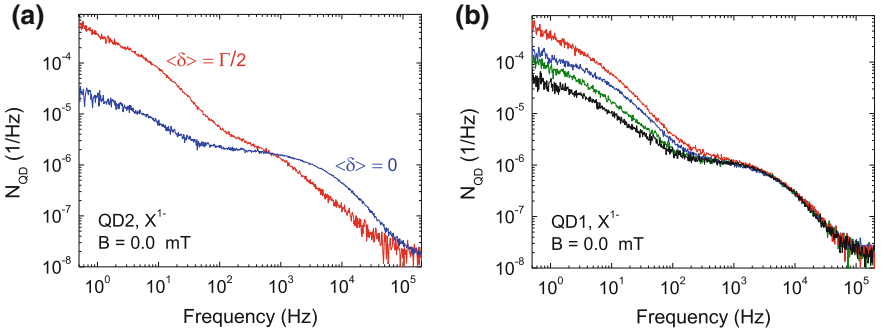

Fig. 9.7 Resonance fluorescence noise. **a** RF noise spectra recorded on a quantum dot occupied with a single electron, the trion X^{1-}, for average detuning equal to zero, $\langle\delta\rangle = 0$ (*blue*), and for $\langle\delta\rangle = \Gamma/2$ (*red*) at 4.2 K and $B = 0.0$ mT. Following the scheme in Fig. 9.8, the noise at low frequencies is shown to originate from charge noise, that at high frequencies from spin noise. Plotted is the noise power spectrum of the normalized RF, $S(t)/\langle S(t)\rangle$, where $S(t)$ is the RF signal, $\langle S(t)\rangle$ the average RF signal, corrected for external sources of noise. **b** RF noise spectra recorded on X^{1-} with $\langle\delta\rangle = 0$ under identical experimental conditions (4.2 K, $B = 0.0$ mT) in the course of the experiment. The charge noise at low frequency depends on the sample history; the spin noise at high frequency does not (color figure online)

Figure 9.7a shows noise spectra over six decades of resolution in the noise power over six decades of frequency, from 0.1 Hz to 100 kHz, Fig. 9.7a, b. The noise falls very rapidly above 10 kHz: this is consistent with the observation of transform-limited linewidths in the spectroscopic measurement on exactly the same quantum

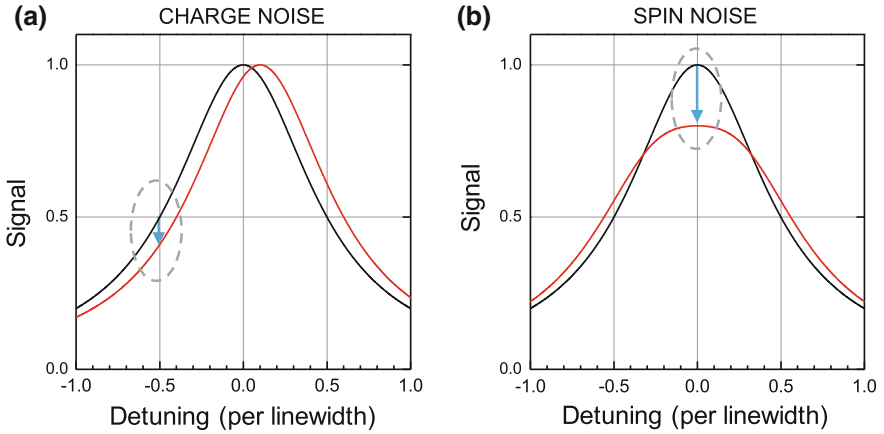

Fig. 9.8 Distinguishing between charge noise and spin noise. Schematic showing the effect of charge noise and spin noise on the charged, X^{1-}, exciton (applied magnetic field zero). **a** Charge noise (noise in the local electric field) results in a "rigid" shift of the optical resonance leading to a small change in resonance fluorescence (RF) for zero detuning $\delta = 0$ and a large change in RF at $\delta = \Gamma/2$. **b** Without an external magnetic field, spin noise induces a Zeeman splitting in the resonance resulting in a large change in RF at $\delta = 0$ and a small change in RF at $\delta = \Gamma/2$ (zero for $\delta = \Gamma/2\sqrt{3}$), opposite to charge noise. This difference, a "rigid" shift of the X^{1-} resonance from charge noise, a "breathing motion" in the X^{1-} resonance from spin noise, allows charge noise and spin noise to be identified

dot, Fig. 9.8c, d. The entire noise spectrum can be described by two Lorentzian features along with a $1/f$-like component. Significantly, there is a spectroscopic technique to assign these noise sources to charge noise or spin noise, Fig. 9.8, based on the different response of X^{1-} to charge noise and spin noise.

As the local electric field F fluctuates, the detuning δ of the quantum dot optical resonance with respect to the constant laser frequency fluctuates on account of the dc Stark effect. For small electric field fluctuations, the Stark shift is linear: the optical resonance shifts rigidly backwards and forwards on the detuning axis, as shown in Fig. 9.8a. The response in the RF to charge noise has a first order component in electric field for $\delta = \Gamma/2$ giving rise to large changes in the RF. Conversely, for $\delta = 0$ the first order component vanishes. Sensitivity to charge noise in the RF is therefore weak for $\langle\delta\rangle = 0$ yet strong for $\langle\delta\rangle = \Gamma/2$. Spin noise results in a complementary behaviour in the absence of an external magnetic field, $B = 0$. Fluctuations in the local magnetic field B_N arising from spin noise do not shift the X^{1-} resonance backwards and forwards. Instead, a typical B_N fluctuation induces a sub-linewidth Zeeman splitting of the X^{1-} resonance, as shown in Fig. 9.8b. Sensitivity to spin noise in the RF is therefore strong for $\langle\delta\rangle = 0$, weak for $\langle\delta\rangle = \Gamma/2$. The crucial point is that, for X^{1-} at $B = 0$, the dependence of the RF noise on $\langle\delta\rangle$ is *opposite* for charge noise and spin noise.

The detuning dependence, Fig. 9.7a, therefore identifies the main noise at low frequencies (Lorentzian spectrum and $1/f$-like component) as charge noise, the

main noise at high frequencies spin noise. The charge noise gives large noise powers but only at low frequencies. The spin noise gives much weaker noise powers but over a much larger bandwidth. It is striking that the resonance fluorescence reveals the full spectrum of the fluctuating nuclear spin ensemble.

The simple rules connecting RF intensity with the local electric field F (charge noise) and with the local magnetic field B_N (spin noise) allow quantitative statements on the noise to be made. The charge noise has root-mean-square (rms) electric field noise $F_{rms} = 0.46\ \mathrm{Vcm}^{-1}$ (bandwidth starting at 0.1 Hz). It is striking that, first, the charge noise is very small: the rms noise in the local potential is just 1.2 μV; the charge noise contribution to the low-scanning-frequency X^{1-} linewidths are $<0.05\,\mu\mathrm{eV}$. The low charge noise is a consequence of both the ultra-pure material and also the carefully controlled experimental conditions. Secondly, it is striking that the charge noise is concentrated at such low frequencies. The rms noise in the Overhauser field measured on X^{1-} amounts to $B_{N,rms} = 9$ mT with correlation time 100 μs. It is this noise which makes the dominant contribution to the X^{1-} linewidth at low scanning frequency. The random fluctuations of N nuclear spins lead to a $B_{N,rms}$ which scales as $1/\sqrt{N}$ [46, 47]; applied to an InGaAs quantum dot with $N \sim 10^5$, the expectation is $B_{N,rms} \sim 20$ mT [57, 58], reasonably close to the value measured here. The timescale is characteristic of the nuclear spin dipole-dipole interaction [46].

Figure 9.8b shows $N_{QD}(f)$ curves measured on the same quantum dot over the course of the experiment (several months) under nominally identical conditions. There are changes in the low frequency noise power (up to a factor of 10) but the high frequency noise remains exactly the same. The charge noise therefore depends on the sample's history. Conversely, the spin noise arises from the host nuclear spins of the quantum dot which remain the same and retain their properties: this results in the unchanging spin noise at high frequency.

A Lorentzian noise spectrum is characteristic of a two-level fluctuator [59]. The associated on-off behaviour, equivalently telegraph noise, is however not observed here. Instead, the Lorentzian noise arises from fluctuations in an *ensemble* of two-level fluctuators, each with approximately the same transition rates, $0 \rightarrow 1$, $1 \rightarrow 0$. For the charge noise, the fluctuators are hole localization centres at an interface 150 nm above the quantum dot. Electrostatic noise arises via fluctuations in the exact configuration of occupied (state 0) and unoccupied (state 1) localization sites in the ensemble. For the spin noise, each nuclear spin acts as a fictitious two-level fluctuator. A Monte Carlo simulation enables both sources of noise to be treated on an equal footing [28]. The $1/f$-like noise varies from quantum dot to quantum dot and its exact origin is an open question.

9.3.2 The Neutral Exciton

There is evidence that at low temperature, there is negligible pure upper level decoherence of the neutral exciton [35, 41–43]. Photons emitted subsequently are close to indistinguishable [39, 60]. The experiments described above add weight to these

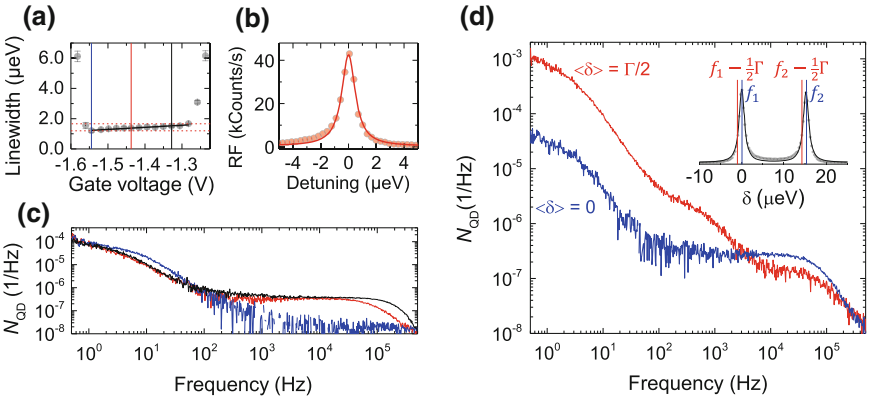

Fig. 9.9 X^0 **spin noise within the Coulomb blockade plateau**. **a** X^0 optical linewidth measured at Rabi energy $\Omega/\Gamma_0 = 0.50$ for different gate voltages by sweeping the laser frequency through the resonance and integrating 100 ms per point. Γ decreases from 1.66 to 1.19 μeV with decreasing gate voltage. **b** X^0 spectrum with $\Gamma = 1.15$ μeV at $V_g = -1.54$ V. **c** X^0 noise spectra recorded at Rabi energies $\Omega/\Gamma_0 = 0.65$ for different voltages, indicated in **a** by *solid lines*. Maximum/minimum spin noise (*black/blue*) is correlated with the largest/smallest Γ. **d** $N_{QD}(f)$ on X^0 recorded with two lasers of frequencies f_1 and f_2 and a frequency splitting $f_1 - f_2$ equal to the fine structure splitting for $\langle\delta\rangle = 0$ (*blue*) and $\langle\delta\rangle = \Gamma/2$ (*red*). *Inset* shows the laser frequency detuning relative to the optical resonance

assertions: transform-limited linewidths are observed on fast scanning [28, 56]. Charge noise leads to an inhomogeneous broadening of the X^0 as for the X^{1-}, Fig. 9.5. The X^0 is also sensitive to spin noise, i.e. fluctuations in the Overhauser field, but with reduced sensitivity with respect to X^{1-}. For X^0, the sensitivity is second order as the hole "shields" the electron from the spin noise (a consequence of the fine structure); for X^{1-} the sensitivity is first order on account of the unpaired electron in the X^{1-} ground state. Despite the different sensitivity to spin noise the X^0 and X^{1-} linewidths are very similar [23, 24, 28].

A typical X^0 resonance fluorescence spectrum is shown in the ideal case (high quality material at low temperature, resonant excitation on a quantum dot in the Coulomb blockade regime) in Fig. 9.5 with $\Omega/\Gamma_0 = 0.5$ where Ω is the Rabi coupling. The linewidth is a factor of 1.4 larger than the transform-limit (for this particular quantum dot, $\Gamma_0^{X^0} = 0.92 \pm 0.10$ μeV). Figure 9.9a shows Γ versus V_g on X^0, measured below but close to saturation, $\Omega/\Gamma_0 = 0.5$. At the edges of the Coulomb blockade plateau, Γ rises rapidly on account of fast electron spin dephasing via co-tunneling with the Fermi sea [17]. This process slows down as V_g moves away from the plateau edges. The prominent feature is that a "sweet-spot" exists close to the negative V_g-end of the plateau with minimum linewidth 1.19 ± 0.13 μeV, Fig. 9.9a, b. Accounting for the small power broadening, the ideal limit is $\Gamma(\Omega) = \Gamma_0[1 + 2(\Omega/\Gamma_0)^2]^{\frac{1}{2}} = 1.10 \pm 0.10$ μeV. Within the measurement uncertainties of 10%, the transform-limit is therefore achieved. As V_g is raised to the positive side of the "sweet-spot", Γ increases beyond the ideal limit, Fig. 9.9a.

As for the X^{1-}, a diagnostic of the X^0 linewidth is a noise spectrum $N_{QD}(f)$, a Fourier transform of the RF time-trace. The increase in linewidth above the transform-limit represents a sum over all noise sources from the scanning frequency, about 1 Hz, to $\Gamma_0/\hbar$, about 1 GHz. The noise spectra at the low-bias end (the "sweet-spot"), the centre of the plateau and the positive-bias end are shown in Fig. 9.9c. There is a Lorentzian feature with linewidth 30 Hz (noise correlation time 30 ms) and a second Lorentzian feature at higher frequencies with linewidth 200 kHz (correlation time 5 μs). The second feature disappears at the "sweet-spot".

A spectroscopic diagnostic for charge versus spin noise can be established, as for the X^{1-}. Now however two lasers are required: one laser drives one of the X^0 transitions, the other laser drives the other X^0 transition. The scheme exploits the different X^0 response to charge noise and spin noise: charge noise moves both X^0 peaks rigidly together along the detuning axis; spin noise moves them apart or closer together, a "breathing" motion. Specifically, X^0 noise spectra are recorded with two lasers whose frequencies are separated by the fine structure. On detuning both lasers from $\delta = 0$ to $\delta = \Gamma/2$, the sensitivity to charge noise increases (changing from second order to first order) yet the sensitivity to spin noise decreases (remaining second order but with a reduced pre-factor). In the experiment, switching from $\langle\delta\rangle = 0$ to $\langle\delta\rangle = \Gamma/2$ causes the noise power of the low frequency component to increase markedly, Fig. 9.9d, identifying it as charge noise. However, as for X^{1-}, the frequency-sum over the charge noise gives a contribution to Γ of $<0.05\,\mu$eV, a negligible value. (Note that both the dc Stark coefficient and Γ vary from quantum dot to quantum dot yet there is no correlation between the two, pointing also to the unimportance of charge noise in the optical linewidth.) Conversely, the noise power of the high frequency component decreases on detuning both lasers from $\delta = 0$ to $\delta = \Gamma/2$, identifying it as spin noise, Fig. 9.9d. Furthermore, noise spectra measured at $\langle\delta\rangle = 0$ but with a single laser tuned to one of the X^0 transitions show that the low frequency noise, the charge noise, is similar for all three biases yet the high frequency noise, the spin noise, increases with increasing bias, Fig. 9.9c. This confirms that the high frequency noise, the spin noise, is responsible for the inhomogeneous linewidth: the integrated spin noise is vanishingly small at the "sweet-spot", increasing at the centre of the plateau, and increasing further at the positive bias edge.

The "spin noise" of the X^0 is not understood microscopically. If the noise is assigned entirely to an Overhauser field, B_N, very large values are required to account for the experimental results, hundreds of mT, with values increasing with optical Rabi coupling: optical driving apparently agitates the nuclei. Also, the correlation time of the noise is just 5 μs (independent of optical Rabi coupling), considerably smaller than the timescale typical of the nuclear spin-nuclear spin dipole-dipole interaction. An alternative is to parameterize the X^0 spin noise as a B_N-induced fluctuation of the fine structure splitting. This however remains conjecture. The experiment demonstrates only that there is noise in the frequency separation of the two X^0 transitions. This speculation notwithstanding, the "spin noise" disappears at the "sweet spot" and this is a robust phenomenon occurring on all the quantum dots investigated in this sample [56].

9.3.3 Locking the Quantum Dot Optical Resonance to a Frequency Standard

Unlike a real atom, the exact transition wavelength of a quantum dot is not locked to any particular wavelength and varies considerably from quantum dot to quantum dot. However, the host semiconductor can be designed so that considerable possibilities for tuning the emission wavelength exist. Electric field tuning [61, 62] and strain tuning [63, 64] allow the emission wavelength to be tuned over several nanometres. A major problem remains. As shown above, the emission wavelength is not constant: it varies randomly over time, even in very controlled environments at low temperature. As shown in the noise analysis, the culprit at low frequency is electrical noise in the semiconductor which shifts the emission wavelength via the Stark effect [28]. This noise has a $1/f$-like power spectrum resulting in, first, large and uncontrolled drifts at low frequencies and second, an undefined mean value. This noise, while poorly understood, is ubiquitous in semiconductors and makes it very difficult to couple an individual quantum dot to another quantum system, another quantum dot for instance, or an ensemble of cold atoms. Described here is a scheme to lock the quantum dot emission frequency to a frequency standard [65].

The output of the device is a stream of single photons generated by resonance fluorescence (RF) from a single quantum dot. A sketch of the experimental concept is shown in Fig. 9.10a. A linearly-polarized resonant laser is focused onto the sample surface and drives the optical transition. The resonance fluorescence of the quantum dot is collected with the polarization-based dark field technique [23, 27–29, 42], Fig. 9.10b. Simultaneously, the optical resonance is detected in transmission [24] by superimposing a sub-linewidth modulation to the gate, Fig. 9.10c. The transmission signal arises from an interference of quantum dot scattering with the driving laser [6]. The incoherent part, i.e. the spontaneous emission, averages to zero in transmission; what is detected instead is the coherent scattering, i.e. the Rayleigh scattering. In this way, the experiment utilizes both incoherent and coherent parts of the scattered light, for the single photon output and control, respectively. With a small modulation, the transmission signal has a large slope with zero crossing at zero detuning, Fig. 9.10c, and is therefore ideal for the generation of an error signal. $\Delta T/T$, the error signal, is recorded with a lock-in amplifier to reject noise and the lock-in output is fed into a classical feedback scheme. The feedback output is, like the modulation, applied to the gate electrode of the device. The set-point of the control loop is the zero crossing.

The long-term performance of the frequency locking scheme was tested by recording the RF over several hours, Fig. 9.11, without (blue) and with (red) the stabilizing loop. Without feedback, the RF exhibits fluctuations up to a factor of 2 (blue curve). The origin are slow electrical fluctuations in the sample which cause the transition to drift out of resonance with the laser. With feedback, these fluctuations disappear and the RF remains at a constant level (red curve) with noise determined almost entirely from shot noise in the detector, Fig. 9.11b. The average RF signal is a little smaller with feedback because the applied modulation broadens slightly the resonance.

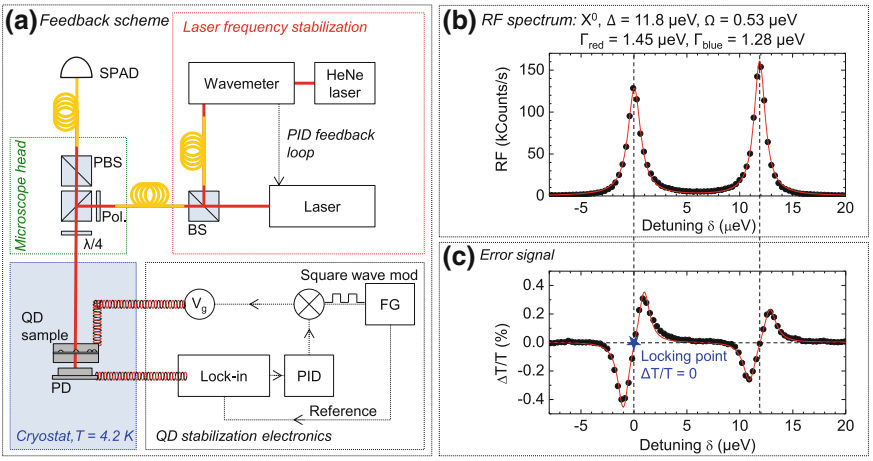

Fig. 9.10 Locking the optical frequency of a single quantum dot to a reference laser: scheme. **a** Schematic view of the experiment. The narrowband laser is stabilized to a fixed frequency by a wavemeter which in turn is stabilized to a HeNe laser. Laser light is guided through optical fibres (*yellow*) and microscope optics before it is focused onto the sample, driving the X^0 transition resonantly (BS = beam-splitter, PBS = polarizing BS, Pol. = linear polarizer). Two simultaneous measurements of X^0 scattering are performed: resonance fluorescence (RF), detected with an avalanche photodiode (APD), and absorption with a photodiode (PD) underneath the sample. The dynamic stabilization is realized with an active PID feedback loop which corrects for fluctuations in the transition energy using the gate voltage V_g and the square wave modulation of a function generator (FG). **b** RF signal of the fine structure split X^0 emission of a single quantum dot at wavelength 936.5 nm, a power corresponding to a Rabi energy Ω of 0.74 μeV and a temperature of 4.2 K. A detuning is achieved by sweeping the gate voltage. The *solid red line* is a Lorentzian fit to the data with linewidth $\Gamma = 1.28$ μeV (309 MHz) and $\Gamma = 1.45$ μeV (350 MHz) and with a fine structure splitting $\Delta = 11.8$ μeV. The linewidths are close to the transform limit of $\Gamma_0 = \hbar/\tau_r = 0.93$ μeV (220 MHz) where τ_r is the radiative lifetime of the exciton transition ($\tau_r = 0.71 \pm 0.01$ ns here). **c** The differential transmission ($\Delta T/T$) signal on the same quantum dot with integration time 100 ms per point using an in situ photodiode. A sub-linewidth square-wave modulation at 527 Hz is applied to the Schottky gate. This broadens both X^0 transitions slightly, here the lower frequency transition from $\Gamma = 1.45$ to $\Gamma = 2.58$ μeV. The *red curve* is a fit to the derivative of the two Lorentzians. The signal around the zero crossing point ($\Delta T/T = 0$) is used to generate an error signal for the feedback scheme. For the PID loop, the proportional factor $P = 0.1$ is chosen with respect to the slope of the error signal, while the integral $I = 0.06$ and the derivative constant $D = 6 \times 10^{-5}$ were obtained by tuning methods (color figure online)

The bandwidth of the feedback can be determined from the RF noise spectrum. $N_{QD}(f)$ corresponding to the time traces of Fig. 9.11a are shown in Fig. 9.11b. Without feedback, $N_{QD}(f)$ has a $1/f$-like dependence on f as a consequence of charge noise in the device, as shown in Fig. 9.7. With feedback, $N_{QD}(f)$ is reduced by up to a factor of 20 at the lowest frequencies, and is constant: the $1/f$-like noise is eliminated. The two curves meet at $f \simeq 130$ Hz once the bandwidth of the PID circuit has been exceeded. At higher frequency the noise spectrum is dominated by spin noise

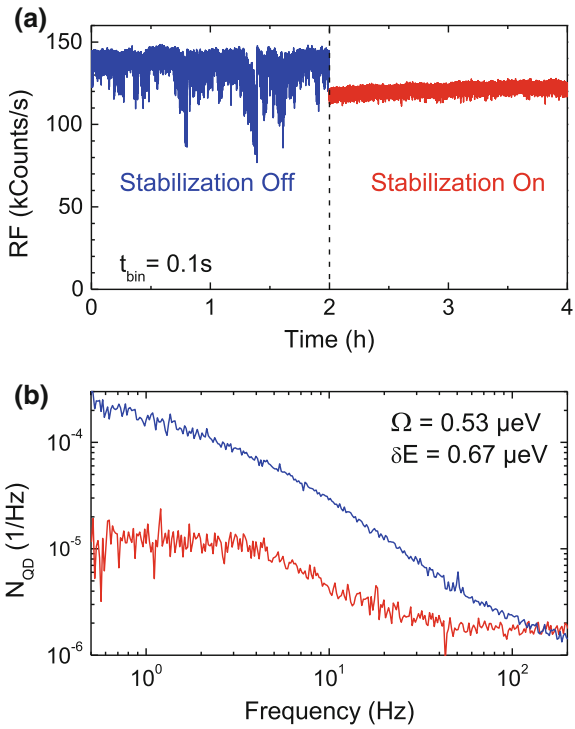

Fig. 9.11 Locking the optical frequency of a single quantum dot to a reference laser: performance. **a** Time trace of the resonance fluorescence (RF) of a single quantum dot (the one from Fig. 9.10) with $\delta = 0$ μeV recorded over several hours. The binning time was $t_{\text{bin}} = 100$ ms. The time trace is plotted with (*red*) and without (*blue*) the dynamic stabilization scheme. **b** Noise spectra of the normalized RF signal, $S(t)/\langle S(t)\rangle$, corresponding to the time traces of **a** after correction for external noise sources (color figure online)

[28] and the PID bandwidth is presently too slow to deal with it. This is however conceivable once the extraction efficiency is much improved.

9.4 Electron Spin Dephasing via the Hyperfine Interaction

A key issue for electron spin dephasing of a spin qubit in GaAs is that an electron spin couples to the nuclear spins in the host material via the contact hyperfine interaction [66], Fig. 9.12. The electron states in a self-assembled quantum dot are constructed from atomic s orbitals, Fig. 9.12b. The large amplitude of the s orbital at the location of each nucleus i results in a Fermi contact hyperfine interaction for an electron spin $\mathbf{S}$ with N nuclear spins $\mathbf{I}_i$

$$H_{\text{hf}}^{e} = \Omega \sum_{j=1}^{N} A_e^j |\Psi_e(\mathbf{R}_j)|^2 (I_z^j S_z + I_x^j S_x + I_y^j S_y). \tag{9.3}$$

A_e^j is the coupling coefficient, Ψ_e the electron envelope function and Ω the unit cell volume. The nuclei create an effective magnetic field, the Overhauser field B_N, which

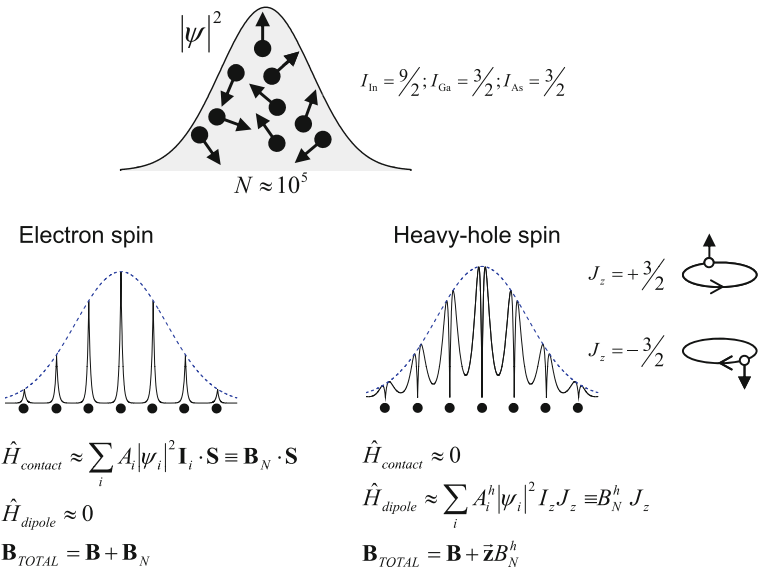

Fig. 9.12 Hyperfine interaction of an electron spin and a hole spin to the nuclear spins in the host material. **a** The electron or hole spin has a wave function extending over a few nm in all three directions such that it overlaps with about $N \sim 10^5$ atoms in the host material, each atom containing a nucleus with non-zero spin in the case of InGaAs. The nuclear spins are given for the main isotopes. **b** The conduction state is constructed largely from atomic *s* orbitals, each localized to a unit cell (shown schematically with the *black line* with the *black circles* representing the nuclei), modulated by the envelope function which extends over the quantum dot (shown schematically with the *blue dashed line*). The contact part of the hyperfine interaction dominates. A_i is the coupling coefficient with nuclear spin i, $\mathbf{I}_i$ the nuclear spin, and ψ_i the electron wave function at the location of nuclear spin i. The contact term resembles the interaction of the electron spin $\mathbf{S}$ in a fictitious magnetic field, $\mathbf{B}_N$. The dipole-dipole hyperfine interaction is zero for a pure *s* orbital, and close to zero in practice. **c** The hole state is constructed largely from atomic *p* orbitals, each localized to a unit cell, such that the wave function amplitude is small at the location of each nucleus. This suppresses the contact part of the hyperfine interaction. The dipole-dipole part is non-zero however. A heavy hole spin has $J_z = \pm\frac{3}{2}$, corresponding, in a semi-classical interpretation, to a circulating microscopic current clockwise with spin up, or counter-clockwise with spin down. The magnetic dipole moment points therefore either along $+z$ or $-z$ such that the dipole-dipole Hamiltonian has an Ising form, $\propto I_z J_z$. Equivalently, the fictitious magnetic field describing the nuclear spins lies solely along the z-direction (color figure online)

fluctuates in time resulting in spin dephasing [46, 47]. For self-assembled quantum dots, $N \sim 10^5$, $B_{\rm N} \sim 20$ mT resulting in an energy fluctuation in the electron Zeeman energy of $\delta E_z \simeq 0.6$ μeV and $T_2^* \sim 1$ ns.

The first order electron spin-nuclear spin flip-flop processes can be suppressed simply by applying a magnetic field, exploiting the mismatch in electron and nuclear gyromagnetic ratios. The interaction along the magnetic field direction remains and leads to the small electron spin T_2^* times [67]. One mitigating strategy is to prepare the nuclear spins carefully [68–70]. Another is to exploit the low frequency of the

nuclear spin dynamics with dynamic decoupling or real-time Hamiltonian estimation methods [52, 70–72], techniques yet to be implemented on self-assembled quantum dots. Optimistically, these first order hyperfine effects can be dealt with. However, the second order processes remain and it has been proposed that they determine the ultimate limit on electron spin coherence [47, 73, 74]. This point is difficult to prove experimentally – many factors (phonons, co-tunneling, charge noise [75]) influence the electron spin decoherence – and the theory is complex [76, 77].

One way to probe the hyperfine interaction between an electron spin and the nuclear spins is to probe the interaction from the point of view of the nuclear spins. In the absence of an electron, the nuclear spins are largely isolated, interacting with each other only by the weak dipole-dipole interaction, leading to long coherence times (milli-second regime) [78, 79]. This is an ideal starting point: the nuclear spin coherence is a sensitive probe of any interaction turned on by the presence of a single electron. Specifically, the second order flip-flop process should lead to a measurable effect on the nuclear spin coherence. The particular process is a spin flip-flop between two nuclear spins. The two nuclear spins are far apart such that they are not coupled by the dipole-dipole interaction. Instead, the coupling is mediated by a common coupling to the delocalized electron. This mechanism couples all nuclear spins together which can conserve energy on undergoing a flip-flop, "shells" of nuclear spins along a contour of constant electron density. In a quantum dot, this electron-mediated nuclear spin-nuclear spin flip-flop couples many nuclear spins together, and the problem has a complex, mesoscopic character.

This approach, addressing the hyperfine-decoherence of the electron spin via the nuclear spin decoherence, hinges on the ability to perform nuclear magnetic resonance (NMR) on the nuclear spins. Self-assembled quantum dots have advantages here. First, the pronounced Coulomb blockade allows the nuclear spin coherence to be measured both with and without an electron. Secondly, the nuclear spins can be both polarized ("dynamic nuclear polarization", DNP) and read-out optically [80]. DNP represents a laser-cooling of the nuclear spins down to mK temperatures [81] creating large population differences amongst the nuclear spin levels, boosting the otherwise very weak NMR signal. A nuclear polarization results in subtle shifts to the optical resonance frequency which can be measured very precisely. Nuclear magnetic resonance sensitive to just ∼1,000 nuclear spins has been achieved [79, 81, 82]. Finally, the nuclei in InGaAs quantum dots have large quadrupole shifts [81–83] and, arguably, this represents a simplification: in an NMR experiment on nuclear spins with $I > \frac{1}{2}$, a narrowband NMR drive selects only one transition and the nuclei can be treated as a collection of spin-$\frac{1}{2}$ spins, an ideal test-bed for theory.

The experiment measures the coherence of the nuclear spins associated with an InGaAs quantum dot for different charge states, empty (0), singly-occupied ($1e$) and doubly-occupied ($2e$). A static magnetic field is applied along the growth direction, z; an oscillating magnetic field is applied in-plane, in the x-direction, by sending a current through an on-chip micro-wire, Fig. 9.13d, e. Specifically, the coherence associated with the "central" transition (nuclear spin $I_z = -\frac{1}{2} \leftrightarrow I_z = +\frac{1}{2}$) of the ^{75}As and ^{115}In isotopes is measured. On account of the in-built strain, each nucleus

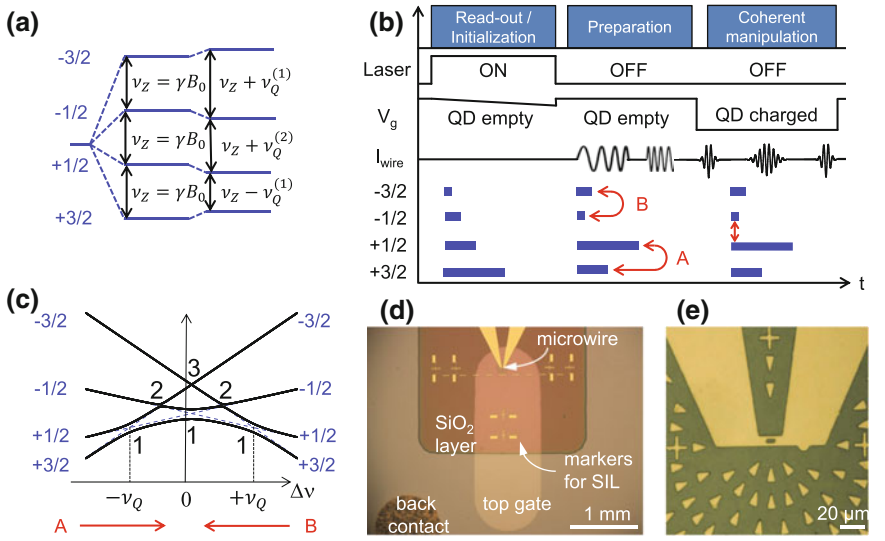

Fig. 9.13 Concepts of the quantum dot NMR experiment. **a** Energy levels for a spin $I = \frac{3}{2}$ in the laboratory frame. The static field B_z causes the spin states to split into the Zeeman ladder with spacing Larmor frequency ν_Z. Quadrupole effects result in alterations to the level spacing; the central transition frequency is only shifted by second order terms. **b** Measurement cycle: *Read-out/initialization* involves detecting resonance fluorescence from the empty quantum dot (neutral exciton) excited with a narrow-band laser: this both reads the previous nuclear spin polarization and sets a new state. In the *Preparation* part, two chirped pulses are applied, A and B, which swap the populations $+\frac{3}{2} \leftrightarrow +\frac{1}{2}$, $-\frac{3}{2} \leftrightarrow -\frac{1}{2}$ in order to maximize the population difference between the $+\frac{1}{2}$ and $-\frac{1}{2}$ states. In the *Coherent manipulation* part, a particular bias (which controls the quantum dot charge) is applied to the gate of the device, and then a pulse of ac current is applied to the microwire at the radio frequency of the central transition. Finally, the bias is re-set to the starting value. **c** Energy levels for a $\frac{3}{2}$ spin in the rotating frame versus radio frequency detuning in the limit of $\nu_Q \gg \nu_{RF}$ where ν_{RF} is the Rabi coupling. The preparation pulses are indicated by red arrows. **d** Top view of sample showing back contact, top gate, SiO_2 spacer layer, microwire and markers for positioning the solid immersion lens (SIL). **e** Zoom-in of the microwire. A hole in the wire enables optical access to the quantum dot; the *triangular markers* facilitate positioning of the sample in the microscope

experiences an electric field gradient which leads to quadrupole shifts of the bare levels [81–83], as shown in Fig. 9.13a, the eigenenergies in the laboratory frame. The in-built strain is site-dependent resulting in a spread of electric field gradients across the quantum dot, in particular across the electron wave function. For ^{75}As with $I = \frac{3}{2}$, the first-order quadrupole effect shifts the $I_z = -\frac{3}{2} \leftrightarrow I_z = -\frac{1}{2}$ transition to lower frequencies, the $I_z = +\frac{1}{2} \leftrightarrow I_z = +\frac{3}{2}$ transition to higher frequencies, yet the frequency of the central transition is shifted only in second-order. The NMR spectrum consists of a central peak at ν_z, inhomogeneously broadened by the second order quadrupole effects, and well-separated sidebands at $\nu_z \pm \nu_Q^{(1)}$ where ν_z is the Zeeman frequency and $\nu_Q^{(1)}$ the first-order quadrupole shift [82]. For ^{115}In with $I = \frac{9}{2}$,

there are 9 NMR transitions but, as for ^{75}As, the central transition is unaffected by the quadrupole interaction to first order. Hence, in the limit $\nu_Q^{(1)} \gg \nu_{\mathrm{RF}}$, for each nuclear spin, the $I_z = -\frac{1}{2} \leftrightarrow I_z = +\frac{1}{2}$ NMR transition can be thought of as a quasi two-level system: on driving at frequency ν_z, population is largely confined to the $I_z = \pm\frac{1}{2}$ sub-space. The eigenenergies in the rotating frame are shown in Fig. 9.13b for a realistic quadrupole frequency $\nu_Q^{(1)}$ (2 MHz) and Rabi coupling ν_{RF} (100 kHz). The strongest avoided-crossings occur when the bare states have a difference in angular momentum of one quantum unit [81].

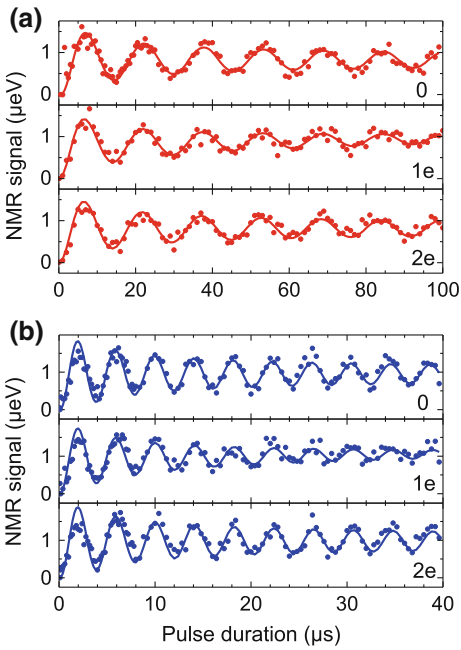

Fig. 9.14 Rabi oscillations of the nuclear spin ensemble. Following nuclear state preparation, the quantum dot is charged (0, 1*e* or 2*e* states) and a radio-frequency pulse resonant with the nuclear central transition is applied. The bias is set to the centre of the charging plateau in the case of an occupancy of one electron. Plotted is the NMR signal (the optical shift) versus pulse duration for **a** arsenic, **b** indium, in each case for occupancy zero, one electron and two electrons. The *solid-lines* represent the calculated response of an inhomogeneous distribution (FWHM of central frequency $\delta\nu_Q^{(2)}$) of two-level emitters with Gaussian distribution of resonance frequency. For ^{75}As, the Rabi coupling is fitted to $\nu_{\mathrm{eff}} = 64$ kHz, $\delta\nu_Q^{(2)} = 71.7$ kHz, radio frequency magnetic field $B_{\mathrm{RF}} = 4.4$ mT from the data at occupancy zero (where T_2 is large, 5 ms). In the 1*e* state, the fit is excellent with the same ν_{eff} and $\delta\nu_Q^{(2)}$ but with $T_2 = 108$ μs. For In, for occupancy zero, the fit yields $\nu_{\mathrm{eff}} = 241$ kHz, $\delta\nu_Q^{(2)} = 146$ kHz and $B_{\mathrm{RF}} = 5.2$ mT. For occupancy of one electron, the fit is excellent with the same ν_{eff} and $\delta\nu_Q^{(2)}$ but with $T_2 = 25$ μs. For both ^{75}As and ^{115}In, the fit for occupancy two electrons is excellent with the same parameters as for occupancy zero. The static magnetic field is $B_z = 6.6$ T, temperature 4.2 K

The measurement protocol is shown in Fig. 9.13b. The nuclear spins are polarized and read-out optically (charge state 0); during the NMR protocol the laser is turned off. Figure 9.14 shows the results of a Rabi oscillation experiment. A pulse at the ^{75}As central transition frequency is applied to the microwire. Figure 9.14a shows the NMR signal as a function of pulse duration. A clear oscillation is observed, a Rabi oscillation, as the population is driven coherently between the $I_z = -\frac{1}{2}$ and $+\frac{1}{2}$ states. The period corresponds closely to the expected result, twice the ^{75}As gyromagnetic ratio (the factor of two is the effective coupling and arises on folding the system to an effective spin-$\frac{1}{2}$ system [84]). When the quantum dot is empty, the Rabi oscillations decay with a time constant of 50 μs. Given that the coherence time associated with this transition is in the ms regime [79], this decay corresponds not to a loss of coherence but to an inhomogeneous broadening, the second-order quadrupole shift to the central transition $\nu_Q^{(2)}$. To determine the inhomogeneous broadening $\delta\nu_Q^{(2)}$, the response of an ensemble of coherent two-level systems with a Gaussian distribution in centre frequencies is calculated. Figure 9.14a shows an excellent fit to the data with $\delta\nu_Q^{(2)} = 71.7$ kHz. When the quantum dot is occupied with a single electron, the Rabi oscillations retain the same frequency but they decay sooner (decay time constant 30 μs). When the quantum dot is occupied with two electrons, the Rabi oscillations behave exactly as for an empty quantum dot. Figure 9.14b shows also a Rabi experiment performed at the ^{115}In central transition. The period of the Rabi oscillations, noticeably smaller than that of ^{75}As, reflects both the different gyromagnetic ratio and the increase in the effective coupling (factor 5 for the spin-$\frac{9}{2}$ ^{115}In). The decay of the Rabi oscillations follows the same pattern as for the isotope ^{75}As:

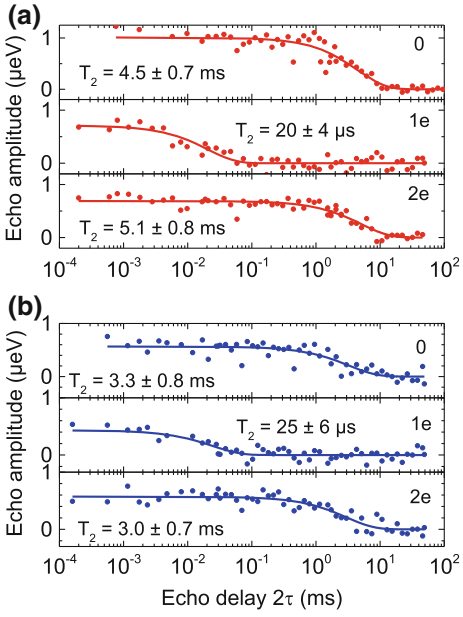

Fig. 9.15 Hahn echo T_2 measurement. NMR signal following a Hahn echo sequence for **a** arsenic, **b** indium, in each case for the three charge states, 0, 1e, 2e. The Hahn echo consists of the standard $\pi/2 - \tau - \pi - \tau - \pi/2$ sequence. The echo amplitude is plotted against the total delay 2τ. Single exponential fits ($\exp(-2\tau/T_2)$) determine the coherence times. T_2 for the singly charged dot is more than a factor 100 lower than for the empty or doubly charged QD

the decay is the same for the empty and doubly-charged states, more pronounced for the single-charged state.

The Rabi oscillations provide the first indication that the nuclear spin dynamics depend on the quantum dot charge. In fact, they reveal a dependence on electron spin: there is a lone spin in the $1e$ state but the two electrons in the $2e$ state form a spin singlet. However, the faster decay of the Rabi oscillations in the presence of a single electron could signify a decreased nuclear spin coherence or an increased ensemble broadening (for instance through the Knight field). To distinguish between these two cases, it is necessary to measure the coherence associated with the nuclear central transition. The Hahn echo is perfect for this as it removes the dependence on the inhomogeneity in the quadrupole shift. Figure 9.15 presents the Hahn echo amplitude as a function of echo delay for both ^{75}As and ^{115}In, in each case for three charge states. The Hahn echo for the $1e$ state was recorded at the centre of the single-electron charging plateau. For both ^{75}As and ^{115}In, a very pronounced dependence on spin is revealed: the Hahn echo decay time (T_2) *decreases* by more than two orders of magnitude in the presence of a lone electron spin.

For an empty quantum dot, T_2 is a few ms for both ^{75}As and ^{115}In, agreeing with previous experiments [79]. The general timescale points to decoherence via a dipole-dipole interaction. For a singly-occupied quantum dot however the T_2 times fall to just $\sim 20\,\mu$s, a timescale far too short for a dipole-dipole interaction, and an additional decoherence mechanism is clearly turned on. Figure 9.16 shows T_2 versus bias, marking the extents of the $1e$ charging plateau. Far from the charging bias, T_2 is independent of bias for the 0 state, falling monotonically as the charging plateau is crossed. T_2 reaches a minimum at the centre of the $1e$ plateau. In fact T_2 is symmetric about the centre of the $1e$ charging plateau, recovering completely in the $2e$ plateau. This is a striking result: the nuclear spins are least coherent in the $1e$ plateau centre when the electronic degrees of freedom (charge, electron spin, exciton) are most coherent.

In the $1e$ plateau, the electron spin relaxation time T_1^e and the nuclear spin relaxation time T_1 follow exactly the opposite dependence on bias as compared to the nuclear spin T_2. T_1^e is very small close to the edges of the $1e$ plateau edge on account of co-tunneling (the quantum dot electron spin relaxes rapidly by swapping its spin with an electron in the Fermi sea) [17, 19, 85]. In the $1e$ plateau centre, co-tunneling is suppressed at low temperature by the gap between the quantum dot ground state and the Fermi energy of the Fermi sea such that T_1^e increases (by about 4 orders of magnitude with respect to the plateau edge [17]). The electron T_1 process determines the nuclear spin T_1 process: nuclear spin leaks into the Fermi sea [86]. This anti-correlation between electron spin relaxation and the nuclear spin coherence is particularly pronounced at the plateau edge itself. Here electron spins relax extremely rapidly (revealed also in an increase in the optical resonance fluorescence linewidth), and the nuclear spin polarization decays relatively quickly. Nevertheless, this rapid electron relaxation has a relatively benign effect on the nuclear spin decoherence. The recovery of the nuclear spin T_2 in the $2e$ state is also completely consistent with this link of nuclear spin coherence to electron spin: in the $2e$ state, the two electrons form a singlet with zero total spin.

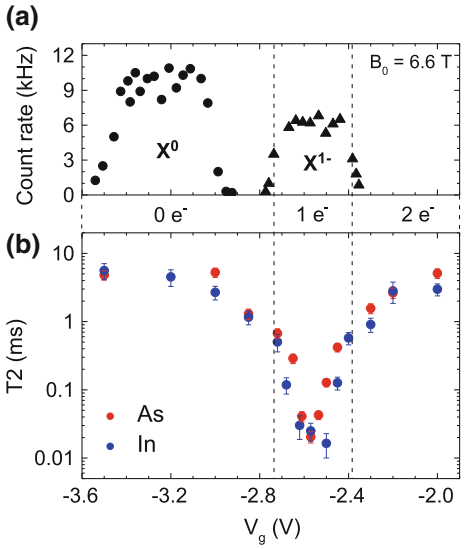

Fig. 9.16 Nuclear spin coherence time as a function of gate voltage. **a** Peak resonance fluorescence intensity for both neutral (X^0) and charged (X^{1-}) excitons versus bias, V_g, for constant laser intensity. *Dashed lines* correspond to an X^{1-} emission intensity drop of 50% and indicate the boundaries of the charging plateau. At the boundary on the "left", the 0 and e states are degenerate and are thus occupied 50:50; equivalently, at the boundary on the "right", the e and $2e$ states are degenerate. **b** Nuclear spin coherence time, T_2, versus bias, V_g

The experiments demonstrate that slow electron spin relaxation promotes nuclear spin decoherence. This points to a nuclear spin-nuclear spin interaction facilitated by a common interaction with an electron spin. Qualitatively, this interaction accounts for the experimental results. First, although this electron-mediated nuclear spin-nuclear spin interaction arises only in second order, it provides a means for many nuclei of a particular isotope in the quantum dot to couple together such that it has significant consequences. Secondly, the interaction is turned off in the $2e$ ground state, a singlet, accounting for the recovery of the nuclear spin coherence in this regime. Thirdly, electron spin relaxation via co-tunneling is fast relative to the nuclear spin dynamics away from the plateau centre such that the nuclear spin ensemble interacts with a time-averaged electron spin $\langle S_z \rangle$. At the edges of the $1e$ plateau, $\langle S_z \rangle$ is small, suppressing the electron-mediated nuclear spin-nuclear spin interaction: this accounts for the anti-correlation between nuclear spin T_2 and electron spin T_1^e.

A quantitative account of the nuclear spin T_2 in the $1e$ plateau centre has been developed [87]. At the plateau centre, the central transitions of a particular isotope represent a closed system, i.e. coupled quasi-spin-$\frac{1}{2}$ spins, as the average quadrupole splittings ($\sim$2 MHz [81]) are larger than the co-tunneling rate ($\sim$0.1 MHz). Provided the electron Zeeman energy is larger than the averaged hyperfine coupling, the electron-mediated nuclear spin-nuclear spin interaction results in a Hamiltonian [74],

$$V = \frac{1}{8Z_e}\sum_{j\neq l} A_j A_l \left[\left(\tfrac{1}{2}+S_z\right)\left(I_j^- I_l^+ + I_l^- I_j^+\right) - \left(\tfrac{1}{2}-S_z\right)\left(I_j^+ I_l^- + I_l^+ I_j^-\right)\right]. \tag{9.4}$$

where Z_e is the electron Zeeman energy (in the total magnetic field, external magnetic field plus Overhauser field), A_j is the hyperfine coupling constant of the jth nuclear spin, S_z is the z-component of the electron spin operator, and I_j is the nuclear spin operator of the jth nuclear spin. The terms $I_j^- I_l^+ + I_l^- I_j^+$ and $I_j^+ I_l^- + I_l^+ I_j^-$ represent nuclear spin-nuclear spin flip-flop processes and these terms lead to nuclear spin decoherence. The dynamics of the transverse components of a single nuclear spin are described in the presence of a coupling to all the others using a master equation to second order in V followed by a calculation of the ensemble decoherence rate. Despite the complexity of the problem, an analytical result for the ensemble decoherence rate $\hat{\Gamma}$ for ^{75}As was derived,

$$\hat{\Gamma}_{\mathrm{As}} = \frac{2\sqrt{2}A_{\mathrm{As}}^3}{9\hbar\omega^2 N}, \tag{9.5}$$

where A_{As} is the hyperfine constant of ^{75}As in GaAs. The total number of nuclear spins in the quantum dot N is known from other experiments [58], $N = (8.5 \pm 0.9) \times 10^4$. The hyperfine coupling, $A_{\mathrm{As}} = 86 \pm 10\,\mu\mathrm{eV}$, is the standard literature value [57, 88]. The Zeeman energy under these conditions, $Z_e = 246 \pm 30\ \mu\mathrm{eV}$, is measured in situ; note that the condition $A < Z_e$ is met in the experiment. The final theoretical result is that $1/\hat{\Gamma}_{\mathrm{As}} = 17 \pm 5\,\mu\mathrm{s}$. The error specified represents a random error arising from the uncertainties in the input parameters. The experimental result for ^{75}As in the plateau centre is $T_2 = 20 \pm 4\ \mu\mathrm{s}$, Fig. 9.16: the experimental and theoretical results agree well. Away from the plateau centre, the co-tunneling rate increases above $\nu_Q^{(1)}$ eventually becoming larger than the total spread in ν_z (50 MHz in this experiment) such that all transitions of all nuclei can in principle be coupled together via the common interaction with the electron; in practice, the co-tunneling rapidly reduces $\langle S_z\rangle$, shutting off the interaction. A complete theory in the co-tunneling regime is formidably complex. This comment notwithstanding, the agreement with the theoretical result at the plateau centre adds considerable weight to the assertion that an electron-mediated interaction is responsible for the decoherence of the nuclear spins in the presence of a single electron.

The overriding point is that probing the nuclear spins in the quantum dot turns out to be a sensitive probe of the interactions turned on by the presence of a single electron. Here, the loss of nuclear spin coherence can be attributed unambiguously to an electron-mediated nuclear spin-nuclear spin coupling. In turn, the prediction is that this interaction limits the electron spin coherence, to time-scales of tens of microseconds in these quantum dots at these magnetic fields. This mechanism determines a hard limit on the electron spin coherence time. The decoherence time can only be increased by increasing the Zeeman splitting (by applying larger magnetic fields or by engineering the electron g-factor) or by increasing the quantum dot size, both hard to achieve in practice.

9.5 Hole Spin Dephasing

The nuclear spins in GaAs lead to a rapid loss of electron spin coherence (both T_2 and T_2^* processes) [2, 46, 47]. Clearly, an approach which retains the GaAs system while suppressing the interaction of the spin qubit to the nuclear spins is attractive. A hole spin offers an alternative platform.

A hole is the absence of an electron in an otherwise occupied valence level. A hole spin has a fundamentally different hyperfine interaction to the electron spin. The valence states are constructed from atomic p orbitals with zero wavefunction amplitude at the location of the nuclei, Fig. 9.12c. The Fermi contact hyperfine interaction is therefore suppressed [2, 89, 90]. The dipole-dipole part of the hyperfine interaction remains [89–92]. For a *pure* heavy hole (HH) state the hyperfine interaction has an Ising form,

$$H_{\rm hf}^{\rm HH} = \Omega \sum_{j=1}^{N} A_{h,z}^{j} |\Psi_h(\mathbf{R}_j)|^2 I_z^j S_z. \tag{9.6}$$

$A_{h,z}^{j}$ is the coupling coefficient, Ψ_h the hole envelope function, and $S_z = \pm\frac{1}{2}$ represents $J_z = \pm\frac{3}{2}$. The absence of transverse terms means that the heavy hole spin experiences just the z-component of the noisy Overhauser field, Fig. 9.12c. Furthermore, the heavy hole coupling coefficients are reduced with respect to the electron coupling coefficients: $A_{h,z}^{j}/A_e^j \simeq -10\%$ [90, 92]. The most important consequence of the Ising form is that application of a transverse magnetic field suppresses hole spin dephasing by the nuclear spins [90]. This is so effective that the hyperfine interaction is to all intents and purposes switched off for a *pure* heavy hole spin [93].

A close-to-ideal heavy hole state exists in unstrained, highly confined GaAs quantum wells [94, 95]. Quantum dots however have mixed states. Even for an ideal quantum dot shape, symmetry does not prevent heavy hole-light hole coupling [96, 97], and heavy hole-light hole coupling is an experimental fact [19, 98–100], revealed by deviations in the optical selection rules from the heavy hole limit. For strained InGaAs quantum dots, the light hole accounts for 5–10% of the hole state [19, 98, 100].

The light hole component in the quantum dot hole state has important consequences for the hole spin hyperfine coupling [92, 93, 101, 102]. Additionally, admixture of the conduction s orbitals should be taken into account [93, 101]: while s admixture is small on account of the fundamental energy gap of the semiconductor, it turns on the large Fermi contact part of the Hamiltonian. In a **k**.**p**-description, the band admixtures are described by an 8×8 Hamiltonian (conduction, heavy hole, light hole and spin-orbit split-off states); the hyperfine interaction consists of a Fermi contact term and dipole-dipole-like interactions [90, 92]. For the hole states, provided the admixtures of light hole and conduction states are small, the hyperfine interaction can be folded down to an effective 2×2 Hamiltonian which operates on the mixed hole states. The two mixed hole states are described as a spin-$\frac{1}{2}$ pseudospin, **S**: $S_z = +\frac{1}{2} \equiv |\Uparrow\rangle$ represents one of the mixed states, $S_z = -\frac{1}{2} \equiv |\Downarrow\rangle$ represents

the other. The final result is that the hole hyperfine interaction is no longer purely Ising-like:

$$H_{\mathrm{hf}}^{h} = \Omega \sum_{j=1}^{N} |\Psi_h(\mathbf{R}_j)|^2 (A_{h,z}^{j} I_z^j S_z + A_{h,x}^{j} I_x^j S_x + A_{h,y}^{j} I_y^j S_y). \tag{9.7}$$

$A_{h,x}^{j}$ and $A_{h,y}^{j}$ are the transverse coupling coefficients and arise from the admixture of both conduction [93, 101] and light hole states [92, 93, 101, 102], both couplings giving terms with the same functional form. In each case, $A_{h,x}^{j}$ and $A_{h,y}^{j}$ depend on $A_{h,z}^{j}$ multiplied by an admixture coefficient. The heavy hole-light hole coupling also introduces non-colinear terms [102]. The transverse coupling makes the hole spin vulnerable to spin dephasing via the in-plane components of the nuclear spins, an interaction which cannot be suppressed in an in-plane magnetic field. In fact the *anisotropy* (rather than the magnitude of $A_{h,z}^{j}$) represents a crucial issue in the development of a hole spin qubit.

Experiments have established long hole spin relaxation times [20, 103–105], coherence times T_2 in the μs range [106, 107], fast spin rotations [107–109] (see Chap. 10) and control of two tunnel-coupled hole spin qubits [108]. The hole spin T_2 falls rapidly above 10 K, a consequence of a spin-orbit mediated phonon interaction [110]. Conveniently, 4 K is cold enough to achieve a highly coherent hole spin. The existence of the longitudinal hole hyperfine interaction has been established [91]. Experimentally, $A_{h,z}^{j}$ averaged over the quantum dot, $\langle A_{h,z} \rangle$, has been measured to be -10% of the average value of A_i^e, $\langle A_i^e \rangle$, on self-assembled quantum dots by dynamically polarizing the nuclear spins along the z-direction and measuring the changes to the electron and hole Zeeman energies [111–113], confirming theoretical expectations [90, 92] albeit with some discussion on the sign [66, 114].

Two difficulties are encountered in probing the hole spin hyperfine interaction optically. First, optical excitation of a hole spin populates an exciton state consisting of two holes in a singlet state but an unpaired electron spin. In this situation it is not trivial to assign any nuclear spin effects unambiguously to the hole spin given the strong hyperfine interaction of the electron spin. Secondly, p-type devices tend to be considerably noisier than n-type devices yet the hole g-factor is very sensitive to an electric field [115–117] such that charge noise results in spin dephasing [107, 116, 117]: in noisy devices this effect completely obscures the hyperfine couplings.

It is important to reduce radically the charge noise in p-type devices. This has been achieved not only by working with ultra-clean material but also by inverting the standard design, switching from the standard p-i-Schottky structure to an n-i-p device. It is also important to carry out an experiment which is sensitive to the transverse terms in the hole hyperfine interaction. This was achieved by polarizing the nuclear spins along a transverse direction, monitoring the polarization via the lone electron spin in the exciton, and measuring the hole Zeeman splitting Z_h ultra-precisely by means of dark state spectroscopy, i.e. coherent population trapping (CPT) [48, 106, 116, 118, 119]. The combination of a coherent hole spin, resonance fluorescence

detection (RF) [120] and low-noise samples resulted in a spectral resolution in Z_h of just 10 neV (2.4 MHz).

9.5.1 Coherence Population Trapping on a Single Hole Spin in a Quantum Dot

CPT is a useful spectroscopic tool to measure the hole Zeeman energy with high resolution. CPT is a quantum interference in a Λ-system where two ground states are coupled individually by "pump" and "probe" optical fields to a common upper level, Fig. 9.17. Here, the two ground states correspond to the Zeeman-split hole spin states, described as $|\Uparrow\rangle_x$ and $|\Downarrow\rangle_x$, and the upper level to an exciton, $|\Uparrow\Downarrow,\downarrow\rangle_x$ or $|\Uparrow\Downarrow,\uparrow\rangle_x$, where $|\Uparrow\rangle_x$ and $|\Downarrow\rangle_x$ are the eigenstates of the hole pseudospin in the x-basis and $|\uparrow\rangle_x, |\downarrow\rangle_x$ refer to the electron spin states, also in the x-basis, Fig. 9.17. A transverse magnetic field (in the x-direction) establishes the quantization axis and the Λ-system, Fig. 9.17. This applies to a hole spin provided the in-plane g-factor is non-zero: the interference occurs when the frequency difference of the lasers matches the hole Zeeman splitting, the two-photon resonance. A dark state results, revealed by a dip in the probe spectrum. The spectral position of the dip measures Z_h. Specifically, when $\hbar\Omega_1 \ll \hbar\Omega_2 \ll \hbar\Gamma_r$ ($\hbar\Omega_1$, $\hbar\Omega_2$ are the probe and pump couplings, Γ_r the spontaneous emission rate) the CPT dip has width $\hbar\Omega_2^2/\Gamma_r$. The depth of the dip is sensitive to the hole spin coherence: only for $1/T_2 \ll \Omega_2^2/\Gamma_r$ does the emission in the dip go to zero. Hence, provided the hole spin coherence is high enough, the width of the CPT dip can be much less than the optical linewidth, enabling a highly accurate measurement of Z_h. Furthermore, the location of the CPT dip is determined only by the two-photon resonance. CPT is therefore an ideal technique to extract Z_h. Fluctuations in exciton energy (via charge noise and the Overhauser field acting on the electron spin) modify the emission envelope [106, 118] but not the location of the CPT dip.

CPT on a single quantum dot containing a single hole is shown in Fig. 9.17. The new p-type devices are very important: they remove the charge-noise-induced fluctuations of the CPT dip position which plagued earlier experiments [116]. The occupation of the upper level is monitored with high signal:noise by detecting the resonance fluorescence [28, 120], Fig. 9.17b, c. The resonance fluorescence exhibits a Lorentzian envelope with full-width-at-half-maximum (FWHM) 2.5 μeV and a pronounced dip with FWHM 80 neV (19.3 MHz). A zoom-in of the CPT dip is shown in Fig. 9.17c along with CPT from a quantum dot in sample B with CPT dip width 33 neV (8.0 MHz). These spectra enable the determination of Z_h with a resolution of ∼10 neV. The hole g-factor (in-plane magnetic field) is $g_{h,x} = 0.063$ for quantum dot A, $g_{h,x} = 0.035$ for quantum dot B. Averaged over many quantum dots in these samples, $\langle g_{h,x}\rangle = 0.12 \pm 0.10$; in the vertical direction, the hole g-factor is much larger, $\langle g_{h,z}\rangle = 1.22 \pm 0.03$. This is reminiscent of the close-to-ideal heavy hole state in an unstrained quantum well for which $g_{h,x} \ll g_{h,z}$. However, the

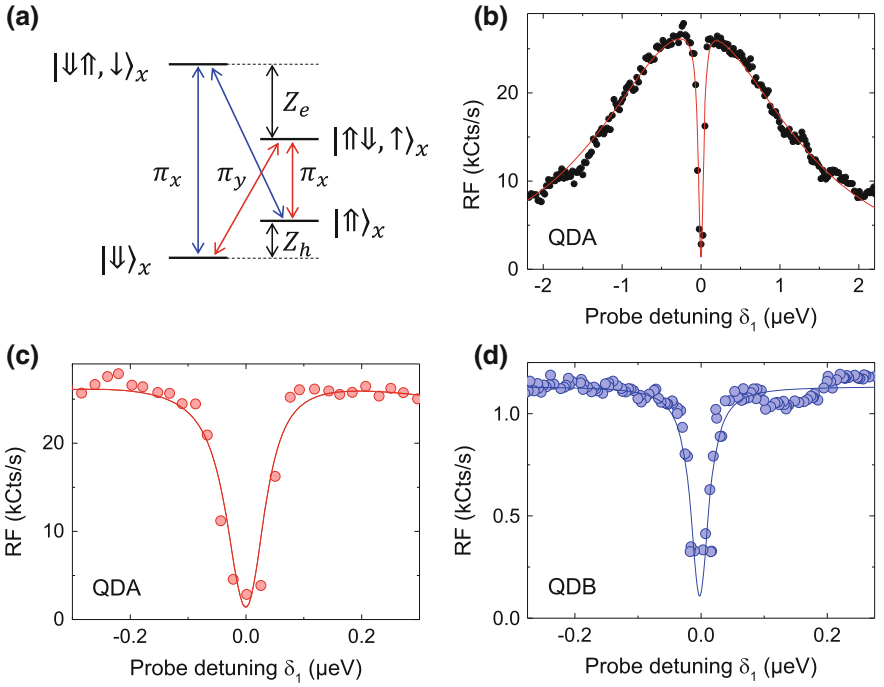

Fig. 9.17 Coherent population trapping on a single hole spin in a quantum dot. **a** The quantum states. Two optical Λ-systems (*blue* and *red lines*) are established in a magnetic field along the x-direction: $|\Uparrow\rangle_x$ and $|\Downarrow\rangle_x$ are the hole pseudospin eigenstates in the x-basis, split by the Zeemann energy Z_h; the upper levels are the X^{1+} excitons consisting of two holes in a singlet state and an unpaired electron with spin $\pm\frac{1}{2}$, again in the x-basis. The optical transitions are linearly polarized, either π_x or π_y, with equal optical dipoles, at wavelengths close to 950 nm. **b** RF spectrum on a single quantum dot QDA containing a single hole in sample A using the "*blue*" Λ-system (pump on higher energy "vertical" transition). The pronounced dip signifies CPT. The *solid line* shows the result of a 3-level density matrix model (probe coupling $\hbar\Omega_1 = 0.06$ μeV, pump coupling $\hbar\Omega_2 = 0.40$ μeV, spontaneous emission rate $\Gamma_r = 0.68$ μeV, $T_2 > 1$ μs, $T_1 \gg T_2$) convoluted with a Lorentzian with FWHM $\Gamma = 2.5$ μeV to describe slow exciton dephasing, and then with a Lorentzian with FWHM 8.3 neV (2.0 MHz) to account for the mutual coherence of the lasers. The data were recorded with 0.1 s integration time per point at a magnetic field $B_x = 3.00$ T and temperature $T = 4.2$ K. **c**, **d** Two exemplary CPT dips of QDA and QDB, respectively. The dip from QDA has a FWHM of 80 neV (19.3 MHz) and is modelled with the parameters of (**b**). The limited mutual coherence of the lasers is the main reason that the signal in the dip centre does not go down completely to zero. The dip from QDB has a FWHM of 33 neV (8.0 MHz), 5 s integration per point. The CPT simulation uses $\hbar\Omega_1 = 0.1$ μeV, $\hbar\Omega_2 = 0.49$ μeV, and, as in **b**, $\Gamma_r = 0.68$ μeV, $T_2 > 1$ μs, $T_1 \gg T_2$. In this case, the remaining signal in the dip centre is likely to be a consequence of the small value of Z_h: the dark state can be destroyed by the weak coupling of the pump to the probe transition (color figure online)

magnitude of $g_{h,x}$ is an unreliable measure of the heavy hole-light hole admixture as $g_{h,x}$ is very sensitive to the indium concentration via the strong dependence of the

band structure parameters on indium concentration [117]. A small $g_{h,x}$ is encouraging but in itself does not represent a suppressed hole spin hyperfine interaction.

The transverse hole hyperfine interaction is measured by combining CPT and DNP. At zero magnetic field, the resonance fluorescence spectra have a straightforward Lorentzian lineshape, Fig. 9.1. This can change in an applied magnetic field where the resonance has a "top-hat" shape extending over tens of μeV and a strong hysteresis on reversing the scan direction [111, 121, 122]. The interpretation is that as the laser is tuned, the nuclei polarize in such a way that resonance with the laser is maintained. This effect, referred to as "dragging", occurs also here and is used as a tool to create a large DNP. Dragging arises through the hyperfine interaction of the lone electron spin in the exciton. Furthermore, the exact change in electron Zeeman energy under DNP can be probed spectroscopically by measuring a change in transition energy of one of the exciton transitions.

In the experiment, the DNP is controlled via the detuning δ_2 of the pump laser with respect to the bare transition frequency. A strong constant frequency pump laser defines the nuclear spin state and a weak probe laser ($\Omega_1 \ll \Omega_2$) measures both Z_h and the electron Zeeman splitting Z_e. The probe laser is scanned across the vertical and diagonal transitions, Fig. 9.18. A pronounced dip in the spectrum indicates CPT and measures Z_h with ultra-high resolution. For zero pump detuning (zero DNP), the probe response at much lower frequencies determines Z_e: an increase in RF is observed when the probe comes into resonance with the lower energy "vertical" exciton transition, $|\Uparrow\rangle_x \rightarrow |\Uparrow\Downarrow, \uparrow\rangle_x$, Fig. 9.18a, b. As the pump is detuned, dragging causes Z_e to change and the change ΔZ_e can be simply monitored via a shift in the exciton transition, Fig. 9.18a, b. Importantly, the probe coupling is lowered in these experiments until the probe itself is too weak to induce DNP, i.e. the frequency of the low energy resonance does not depend on Ω_1. At each pump detuning, equivalently at each value of ΔZ_e, the hole Zeeman energy Z_h is determined with ultra-high resolution by measuring the exact spectral location of the CPT dip, Fig. 9.18a, b. Figure 9.18c, d plots Z_h versus ΔZ_e. Although Z_e changes by almost 20 μeV, Z_h remains constant to within 20 neV for both quantum dots. This is the main result of this experiment: large values of $\langle I_x \rangle$ do not result in a measurable change in Z_h even when Z_h is measured with high resolution.

Quantitatively, this experiment shows that $|\Delta Z_h/\Delta Z_e| < 0.1\%$ in the presence of a transverse DNP. This result can be interpreted in terms of averaged hyperfine couplings, $\Delta Z_h/\Delta Z_e \simeq \langle A_{h,x}\rangle/\langle A_e\rangle$. Hence, $|\langle A_{h,x}\rangle/\langle A_e\rangle| < 0.1\%$. Furthermore, with $|\langle A_{h,z}\rangle/\langle A_e\rangle| = 10\%$ [111–113], the anisotropy of the hole spin hyperfine interaction can be quantified, $|\langle A_{h,x}\rangle/\langle A_{h,z}\rangle| < 1\%$. This is consistent with generic theoretical estimates [93, 102]; a full calculation specific to an InGaAs quantum dot including all admixtures is presently lacking. In terms of energies, $|\langle A_{h,x}\rangle| < 0.1$ μeV. This implies a very small energy broadening δZ_h in the presence of un-polarized but noisy nuclei ($\delta Z_e = 600$ neV): $\delta Z_h^{\text{spin}} < 0.6$ neV. The energy broadening arising from the longitudinal coupling, i.e. from $\langle A_{h,z}\rangle$, is sub-neV for all transverse fields above about 500 mT.

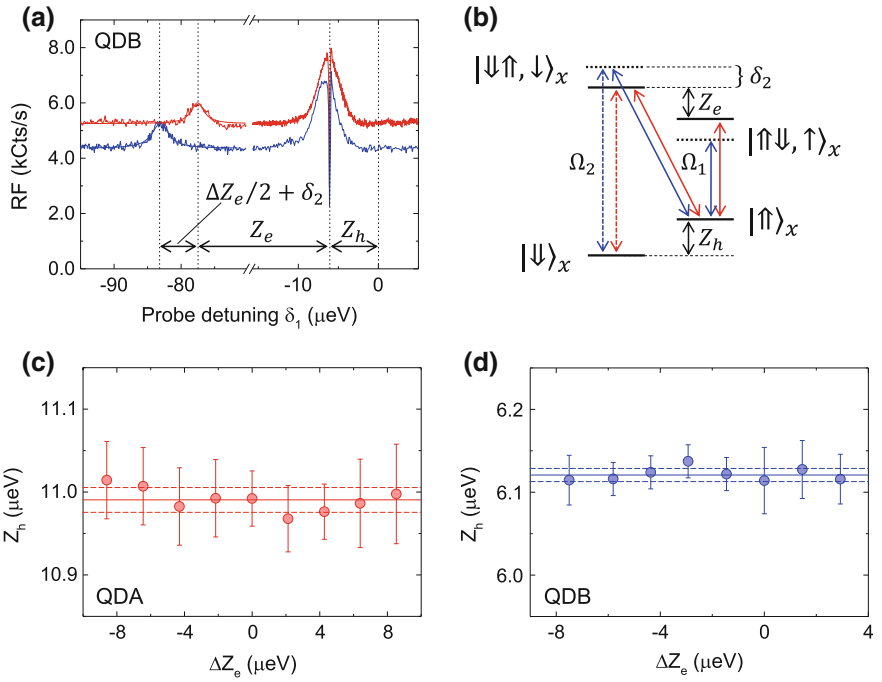

Fig. 9.18 The transverse hyperfine coupling of a single hole spin. **a**, Measured probe RF spectrum on QD B in the presence of a much stronger, constant frequency pump laser, *red*: $\delta_2 = 0$; *blue*: $\delta_2 = 3.4$ μeV. The frequency of the probe laser is scanned across the "vertical" and "diagonal" transitions and is plotted with respect to the pump frequency in both cases. The pronounced dip signifies CPT and occurs when $\delta_1 = Z_h$. The peak at large and negative δ_1 arises when the probe is in resonance with the lower energy "vertical" transition. At $\delta_2 = 0$ the separation between this resonance and the CPT dip determines Z_e, the Zeeman energy of the exciton (determined by the lone electron spin). The shift in this resonance signifies a DNP: Z_e changes in response to the change in pump detuning. The measured Rabi energies are $\hbar\Omega_1 = 0.049$ μeV and $\hbar\Omega_2 = 0.49$ μeV; magnetic field 3.00 T; integration time per point 5 s; temperature 4.2 K. **b** The quantum states of the system: the *red arrows* indicate the optical transitions addressed by scanning the probe laser for $\delta_2 = 0$, *blue* for $\delta_2 > 0$. **c**, **d** Z_h versus the change of the electron Zeeman energy ΔZ_e for samples A (g-factor 0.063) and B (g-factor 0.035), respectively. The *solid line* represents the average value, the *dashed lines* represent $\pm\sigma$ where σ is the standard deviation. At the one-σ level, $dZ_h/d\Delta Z_e = 0.1\%$ (color figure online)

9.5.2 *Hole Spin Dephasing*

The CPT experiments can be used to estimate T_2^*. In a CPT experiment, ensemble broadening (described with a T_2^* time, $T_2^* = \hbar/\delta Z_h$) reveals itself by a lifting of the signal in the dip away from zero and an increase in the dip width. An analysis of the CPT spectra of Fig. 9.17, taking into account the mutual coherence of the lasers, results in an energy broadening $\delta Z_h = 3.3 \pm 2.2$ neV. T_2^* is so large that it is very challenging to measure it with small error. To reduce the error, the CPT result can

be complemented with all the other spectroscopic results. First, the contribution to δZ_h from charge noise is estimated from the noise analysis. Charge noise is particularly small on sample A contributing 0.10 ± 0.05 μeV to the optical linewidth [56] and results in a Z_h fluctuation of $\delta Z_h^{\text{charge}} = 0.3$ neV at $B_x = 3.00$ T. Secondly, the contribution to δZ_h from spin noise can be determined in situ. The X^{1+} linewidth measures the rms fluctuations in electron Zeeman energy, $\delta Z_e = 1.43 \pm 0.07$ μeV at $B_x = 3.00$ T. This noise arises from a fluctuation in the nuclear spin polarization projected along x, the magnetic field direction, and it corresponds to an Overhauser field of ∼40 mT. (Incidentally, this value demonstrates that the nuclear spin distribution is not narrowed in this experiment.) From the upper limit on the coupling coefficient, the corresponding fluctuations in Z_h amount to $<1.43 \pm 0.25$ neV. These results from the linewidths are completely consistent with the CPT result. The final result is that $T_2^* > (460 \pm 80)$ ns.

The long value of hole spin T_2^* arises from the application of an in-plane magnetic field to suppress the longitudinal hyperfine interaction; a very small transverse hyperfine interaction; and low levels of charge noise to reduce charge-noise-induced-dephasing. This T_2^* value is considerably larger than others reported in other experiments [107–109]: it is likely that this is entirely related to the different levels of charge noise in the various experiments. T_2^* is limited by charge and spin noise. In both cases, most of the noise lies at frequencies below 100 kHz [28] such that dynamical decoupling schemes are likely to be highly effective at prolonging the usable coherence beyond T_2^*. Additionally, the nuclear spin coupling can be reduced even further by fabricating flatter quantum dots with circular cross-section to reduce the heavy hole-light hole admixture. A realistic prospect is to push T_2^* into the μs regime. As for a quantum dot electron spin [123], a quantum dot hole spin can be rotated in ∼10 ps [107–109]. This combination makes the hole spin in an InGaAs quantum dot an attractive platform. As described in Chap. 12, hole spin-hole spin entanglement has been achieved.

9.6 Conclusions

A self-assembled quantum dot is, under the right conditions (high quality material at low temperature, resonant excitation on a quantum dot in the Coulomb blockade regime), a close-to-ideal emitter of single photons. The noise experiments show that a quantum dot can emit a train of micro-second duration containing photons whose indistinguishability is very high. The train can be prolonged under certain conditions. An electron spin trapped in a self-assembled quantum dot is dephased by the nuclear spins leading to short T_2^* times and T_2 times in the tens of micro-second regime. This interaction can however be very effectively suppressed by applying an in-plane magnetic field to a hole spin. In the presence of noisy nuclear spins, a hole spin is a superior spin qubit using a self-assembled quantum dot as host provided the charge noise is low.

Acknowledgements All this work was carried out by the first generation of researchers in the Nano-Photonics Group, Department of Physics, University of Basel, Switzerland: Lukas Greuter, Julien Houel, Andreas Kuhlmann, Mathieu Munsch, Jonathan Prechtel and Gunter Wüst. The excellent samples were fabricated by Arne Ludwig and Andreas Wieck at Ruhr-University Bochum, Germany. Franziska Maier and Daniel Loss (Department of Physics, University of Basel) carried out the calculations of the nuclear spin coherence. The work on NMR was carried out as part of a fruitful collaboration with Martino Poggio (also Department of Physics, University of Basel).

References

1. J. Fischer, D. Loss, Science **324**, 1277 (2009)
2. R.J. Warburton, Nat. Mater. **12**, 483 (2013)
3. J.M. Garcia, T. Mankad, P.O. Holtz, P.J. Wellman, P.M. Petroff, Appl. Phys. Lett. **72**, 3172 (1998)
4. W. Langbein, P. Borri, U. Woggon, V. Stavarache, D. Reuter, A.D. Wieck, Phys. Rev. B **69**, 161301 (2004)
5. P.A. Dalgarno, J.M. Smith, J. McFarlane, B.D. Gerardot, K. Karrai, A. Badolato, P.M. Petroff, R.J. Warburton, Phys. Rev. B **77**, 245311 (2008)
6. K. Karrai, R.J. Warburton, Superlattices Microstruct. **33**, 311 (2003)
7. J. Claudon, J. Bleuse, N.S. Malik, M. Bazin, P. Jaffrennou, N. Gregersen, C. Sauvan, P. Lalanne, J.M. Gerard, Nat. Photonics **4**, 174 (2010)
8. D. Loss, D.P. DiVincenzo, Phys. Rev. A **57**, 120 (1998)
9. A. Greilich, D.R. Yakovlev, A. Shabaev, A.L. Efros, I.A. Yugova, R. Oulton, V. Stavarache, D. Reuter, A. Wieck, M. Bayer, Science **313**, 341 (2006)
10. S.A. Crooker, J. Brandt, C. Sandfort, A. Greilich, D.R. Yakovlev, D. Reuter, A.D. Wieck, M. Bayer, Phys. Rev. Lett. **104**, 036601 (2010)
11. H. Drexler, D. Leonard, W. Hansen, J.P. Kotthaus, P.M. Petroff, Phys. Rev. Lett. **73**, 2252 (1994)
12. R.J. Warburton, C. Schaflein, D. Haft, F. Bickel, A. Lorke, K. Karrai, J.M. Garcia, W. Schoenfeld, P.M. Petroff, Nature **405**, 926 (2000)
13. J.H. Prechtel, A.V. Kuhlmann, J. Houel, A. Ludwig, S.R. Valentin, A.D. Wieck, R.J. Warburton, Nat. Mater. **15**, 981 (2016)
14. P.A. Dalgarno, M. Ediger, B.D. Gerardot, J.M. Smith, S. Seidl, M. Kroner, K. Karrai, P.M. Petroff, A.O. Govorov, R.J. Warburton, Phys. Rev. Lett. **100**, 176801 (2008)
15. B.D. Gerardot, R.J. Barbour, D. Brunner, P.A. Dalgarno, A. Badolato, N. Stoltz, P.M. Petroff, J. Houel, R.J. Warburton, Appl. Phys. Lett. **99**, 243112 (2011)
16. S. Seidl, M. Kroner, P.A. Dalgarno, A. Högele, J.M. Smith, M. Ediger, B.D. Gerardot, J.M. Garcia, P.M. Petroff, K. Karrai, R.J. Warburton, Phys. Rev. B **72**, 195339 (2005)
17. J.M. Smith, P.A. Dalgarno, R.J. Warburton, A.O. Govorov, K. Karrai, B.D. Gerardot, P.M. Petroff, Phys. Rev. Lett. **94**, 197402 (2005)
18. M. Atatüre, J. Dreiser, A. Badolato, A. Högele, K. Karrai, A. Imamoglu, Science **312**, 551 (2006)
19. J. Dreiser, M. Atatüre, C. Galland, T. Mueller, A. Badolato, A. Imamoglu, Phys. Rev. B **77**, 075317 (2008)
20. B.D. Gerardot, D. Brunner, P.A. Dalgarno, P. Ohberg, S. Seidl, M. Kroner, K. Karrai, N.G. Stoltz, P.M. Petroff, R.J. Warburton, Nature **451**, 441 (2008)
21. J. McFarlane, P.A. Dalgarno, B.D. Gerardot, R.H. Hadfield, R.J. Warburton, K. Karrai, A. Badolato, P.M. Petroff, Appl. Phys. Lett. **94**, 093113 (2009)
22. N.A.J.M. Kleemans, J. van Bree, A.O. Govorov, J.G. Keizer, G.J. Hamhuis, R. Notzel, A.Y. Silov, P.M. Koenraad, Nat. Phys. **6**, 534 (2010)

23. J. Houel, A.V. Kuhlmann, L. Greuter, F. Xue, M. Poggio, B.D. Gerardot, P.A. Dalgarno, A. Badolato, P.M. Petroff, A. Ludwig, D. Reuter, A.D. Wieck, R.J. Warburton, Phys. Rev. Lett. **108**, 107401 (2012)
24. A. Högele, S. Seidl, M. Kroner, K. Karrai, R.J. Warburton, B.D. Gerardot, P.M. Petroff, Phys. Rev. Lett. **93**, 217401 (2004)
25. A. Muller, E.B. Flagg, P. Bianucci, X.Y. Wang, D.G. Deppe, W. Ma, J. Zhang, G.J. Salamo, M. Xiao, C.K. Shih, Phys. Rev. Lett. **99**, 187402 (2007)
26. A.N. Vamivakas, Y. Zhao, C.Y. Lu, M. Atatüre, Nat. Phys. **5**, 198 (2009)
27. S.T. Yilmaz, P. Fallahi, A. Imamoglu, Phys. Rev. Lett. **105**, 033601 (2010)
28. A.V. Kuhlmann, J. Houel, A. Ludwig, L. Greuter, D. Reuter, A.D. Wieck, M. Poggio, R.J. Warburton, Nat. Phys. **9**, 570 (2013)
29. A.V. Kuhlmann, J. Houel, D. Brunner, A. Ludwig, D. Reuter, A.D. Wieck, R.J. Warburton, Rev. Sci. Instr. **84**, 073905 (2013)
30. M. Kroner, S. Remi, A. Hoegele, S. Seidl, A.W. Holleitner, R.J. Warburton, B.D. Gerardot, P.M. Petroff, K. Karrai, Physica E **40**, 1994 (2008)
31. M. Kroner, C. Lux, S. Seidl, A.W. Holleitner, K. Karrai, A. Badolato, P.M. Petroff, R.J. Warburton, Appl. Phys. Lett. **92**, 031108 (2008)
32. A.J. Ramsay, T.M. Godden, S.J. Boyle, E.M. Gauger, A. Nazir, B.W. Lovett, A.M. Fox, M.S. Skolnick, Phys. Rev. Lett. **105**, 177402 (2010)
33. S.M. Ulrich, S. Ates, S. Reitzenstein, A. Löffler, A. Forchel, P. Michler, Phys. Rev. Lett. **106**, 247402 (2011)
34. M. Bayer, A. Forchel, Phys. Rev. B **65**, 041308 (2002)
35. W. Langbein, P. Borri, U. Woggon, V. Stavarache, D. Reuter, A.D. Wieck, Phys. Rev. B **70**, 033301 (2004)
36. P. Borri, W. Langbein, U. Woggon, V. Stavarache, D. Reuter, A.D. Wieck, Phys. Rev. B **71**, 115328 (2005)
37. N. Sangouard, H. Zbinden, J. Mod. Opt. **59**, 1458 (2012)
38. P. Michler, A. Kiraz, C. Becher, W.V. Schoenfeld, P.M. Petroff, L.D. Zhang, E. Hu, A. Imamoglu, Science **290**, 2282 (2000)
39. C. Santori, D. Fattal, J. Vučković, G.S. Solomon, Y. Yamamoto, Nature **419**, 594 (2002)
40. A.J. Shields, Nat. Photonics **1**, 215 (2007)
41. H.S. Nguyen, G. Sallen, C. Voisin, P. Roussignol, C. Diederichs, G. Cassabois, Appl. Phys. Lett. **99**, 261904 (2011)
42. C. Matthiesen, A.N. Vamivakas, M. Atatüre, Phys. Rev. Lett. **108**, 093602 (2012)
43. C. Matthiesen, M. Geller, C.H.H. Schulte, C. Le Gall, J. Hansom, Z. Li, M. Hugues, E. Clarke, M. Atatüre, Nat. Commun. **4**, 1600 (2013)
44. F. Klotz, V. Jovanov, J. Kierig, E.C. Clark, D. Rudolph, D. Heiss, M. Bichler, G. Abstreiter, M.S. Brandt, J.J. Finley, Appl. Phys. Lett. **96**, 053113 (2010)
45. J. Pingenot, C.E. Pryor, M.E. Flatte, Phys. Rev. B **84**, 195403 (2011)
46. I.A. Merkulov, A.L. Efros, M. Rosen, Phys. Rev. B **65**, 205309 (2002)
47. A.V. Khaetskii, D. Loss, L. Glazman, Phys. Rev. Lett. **88**, 186802 (2002)
48. X. Xu, B. Sun, P.R. Berman, D.G. Steel, A.S. Bracker, D. Gammon, L.J. Sham, Nat. Phys. **4**, 692 (2008)
49. D. Press, K. De Greve, P.L. McMahon, T.D. Ladd, B. Friess, C. Schneider, M. Kamp, S. Hoefling, A. Forchel, Y. Yamamoto, Nat. Photonics **4**, 367 (2010)
50. C. Barthel, J. Medford, C.M. Marcus, M.P. Hanson, A.C. Gossard, Phys. Rev. Lett. **105**, 266808 (2010)
51. G. de Lange, Z.H. Wang, D. Riste, V.V. Dobrovitski, R. Hanson, Science **330**, 60 (2010)
52. H. Bluhm, S. Foletti, I. Neder, M. Rudner, D. Mahalu, V. Umansky, A. Yacoby, Nat. Phys. **7**, 109 (2011)
53. B. Alen, F. Bickel, K. Karrai, R.J. Warburton, P.M. Petroff, Appl. Phys. Lett. **83**, 2235 (2003)
54. A.N. Vamivakas, Y. Zhao, S. Fält, A. Badolato, J.M. Taylor, M. Atatüre, Phys. Rev. Lett. **107**, 166802 (2011)

55. C. Schulhauser, D. Haft, R.J. Warburton, K. Karrai, A.O. Govorov, A.V. Kalameitsev, A. Chaplik, W. Schoenfeld, J.M. Garcia, P.M. Petroff, Phys. Rev. B **66**, 193303 (2002)
56. A.V. Kuhlmann, J.H. Prechtel, J. Houel, A. Ludwig, D. Reuter, A.D. Wieck, R.J. Warburton, Nat. Commun. **6**, 8204 (2015)
57. W.A. Coish, J. Baugh, Phys. Stat. Sol. (b) **246**, 2203 (2009)
58. C. Kloeffel, P.A. Dalgarno, B. Urbaszek, B.D. Gerardot, D. Brunner, P.M. Petroff, D. Loss, R.J. Warburton, Phys. Rev. Lett. **106**, 046802 (2011)
59. S. Machlup, J. Appl. Phys. **25**, 341 (1954)
60. O. Gazzano, S. Michaelis de Vasconcellos, C. Arnold, A. Nowak, E. Galopin, I. Sagnes, L. Lanco, A. Lemaître, P. Senellart, Nat. Commun. **4**, 1425 (2013)
61. R.J. Warburton, C. Schulhauser, D. Haft, C. Schäflein, K. Karrai, J.M. Garcia, W. Schoenfeld, P.M. Petroff, Phys. Rev. B **65**, 113303 (2002)
62. A.J. Bennett, M.A. Pooley, R.M. Stevenson, M.B. Ward, R.B. Patel, A.B. de la Giroday, N. Sköld, I. Farrer, C.A. Nicoll, D.A. Ritchie, A.J. Shields, Nat. Phys. **6**, 947 (2010)
63. S. Seidl, M. Kroner, A. Högele, K. Karrai, R.J. Warburton, A. Badolato, P.M. Petroff, Appl. Phys. Lett. **88**, 203113 (2006)
64. K.D. Jöns, R. Hafenbrak, R. Singh, F. Ding, J.D. Plumhof, A. Rastelli, O.G. Schmidt, G. Bester, P. Michler, Phys. Rev. Lett. **107**, 217402 (2011)
65. J.H. Prechtel, A.V. Kuhlmann, J. Houel, L. Greuter, A. Ludwig, D. Reuter, A.D. Wieck, R.J. Warburton, Phys. Rev. X **3**, 041006 (2013)
66. E.A. Chekhovich, M.N. Makhonin, A.I. Tartakovskii, A. Yacoby, H. Bluhm, K.C. Nowack, L.M.K. Vandersypen, Nat. Mater. **12**, 494 (2013)
67. J.R. Petta, A.C. Johnson, J.M. Taylor, E.A. Laird, A. Yacoby, M.D. Lukin, C.M. Marcus, M.P. Hanson, A.C. Gossard, Science **309**, 2180 (2005)
68. D.J. Reilly, J.M. Taylor, J.R. Petta, C.M. Marcus, M.P. Hanson, A.C. Gossard, Science **321**, 817 (2008)
69. X. Xu, W. Yao, B. Sun, D.G. Steel, A.S. Bracker, D. Gammon, L.J. Sham, Nature **459**, 1105 (2009)
70. M.D. Shulman, S.P. Harvey, J.M. Nichol, S.D. Bartlett, A.C. Doherty, V. Umansky, A. Yacoby, Nat. Commun. **5**, 5156 (2014)
71. W.M. Witzel, S.D. Sarma, Phys. Rev. Lett. **98**, 077601 (2007)
72. L. Cywiński, W.M. Witzel, S. Das Sarma, Phys. Rev. Lett. **102**, 057601 (2009)
73. W. Yao, R.B. Liu, L.J. Sham, Phys. Rev. B **74**, 195301 (2006)
74. D. Klauser, W.A. Coish, D. Loss, Phys. Rev. B **78**, 205301 (2008)
75. R. Hanson, L.P. Kouwenhoven, J.R. Petta, S. Tarucha, L.M.K. Vandersypen, Rev. Mod. Phys. **79**, 1217 (2007)
76. W.A. Coish, J. Fischer, D. Loss, Phys. Rev. B **81**, 165315 (2010)
77. A. Faribault, D. Schuricht, Phys. Rev. Lett. **110**, 040405 (2013)
78. Y. Kondo, M. Ono, S. Matsuzaka, K. Morita, H. Sanada, Y. Ohno, H. Ohno, Phys. Rev. Lett. **101**, 207601 (2008)
79. E.A. Chekhovich, M. Hopkinson, M.S. Skolnick, A.I. Tartakovskii, Nat. Commun. **6**, 6348 (2015)
80. B. Urbaszek, X. Marie, T. Amand, O. Krebs, P. Voisin, P. Maletinsky, A. Högele, A. Imamoglu, Rev. Mod. Phys. **85**, 79 (2013)
81. M. Munsch, G. Wüst, A.V. Kuhlmann, F. Xue, A. Ludwig, D. Reuter, A.D. Wieck, M. Poggio, R.J. Warburton, Nat. Nanotechnol. **9**, 671 (2014)
82. E.A. Chekhovich, K.V. Kavokin, J. Puebla, A.B. Krysa, M. Hopkinson, A.D. Andreev, A.M. Sanchez, R. Beanland, M.S. Skolnick, A.I. Tartakovskii, Nat. Nanotechnol. **7**, 646 (2012)
83. C. Bulutay, E.A. Chekhovich, A.I. Tartakovskii, Phys. Rev. B **90**, 205425 (2014)
84. E. Van Veenendaal, B. Meier, A. Kentgens, Mol. Phys. **93**, 195 (1998)
85. M. Kroner, K.M. Weiss, B. Biedermann, S. Seidl, A.W. Holleitner, A. Badolato, P.M. Petroff, P. Öhberg, R.J. Warburton, K. Karrai, Phys. Rev. B **78**, 075429 (2008)
86. P. Maletinsky, A. Badolato, A. Imamoglu, Phys. Rev. Lett. **99**, 056804 (2007)

87. G. Wüst, M. Munsch, F. Maier, A.V. Kuhlmann, A. Ludwig, A.D. Wieck, D. Loss, M. Poggio, R.J. Warburton, Nat. Nanotechnol. **11**, 885 (2016)
88. D. Paget, G. Lampel, B. Sapoval, V.I. Safarov, Phys. Rev. B **15**, 5780 (1977)
89. E. Grncharova, V. Perel, Sov. Phys. Semicond. **11**, 977 (1977)
90. J. Fischer, W.A. Coish, D.V. Bulaev, D. Loss, Phys. Rev. B **78**, 155329 (2008)
91. B. Eble, C. Testelin, P. Desfonds, F. Bernardot, A. Balocchi, T. Amand, A. Miard, A. Lemaître, X. Marie, M. Chamarro, Phys. Rev. Lett. **102**, 146601 (2009)
92. C. Testelin, F. Bernardot, B. Eble, M. Chamarro, Phys. Rev. B **79**, 195440 (2009)
93. J. Fischer, D. Loss, Phys. Rev. Lett. **105**, 266603 (2010)
94. H.W. van Kesteren, E.C. Cosman, W.A.J.A. van der Poel, C.T. Foxon, Phys. Rev. B **41**, 5283 (1990)
95. R.W. Martin, R.J. Nicholas, G.J. Rees, S.K. Haywood, N.J. Mason, P.J. Walker, Phys. Rev. B **42**, 9237 (1990)
96. G. Bester, A. Zunger, Phys. Rev. B **71**, 045318 (2005)
97. J.W. Luo, G. Bester, A. Zunger, Phys. Rev. B **92**, 165301 (2015)
98. D.N. Krizhanovskii, A. Ebbens, A.I. Tartakovskii, F. Pulizzi, T. Wright, M.S. Skolnick, M. Hopkinson, Phys. Rev. B **72**, 161312 (2005)
99. T. Belhadj, T. Amand, A. Kunold, C.M. Simon, T. Kuroda, M. Abbarchi, T. Mano, K. Sakoda, S. Kunz, X. Marie, B. Urbaszek, Appl. Phys. Lett. **97**, 051111 (2010)
100. C.Y. Lu, Y. Zhao, A.N. Vamivakas, C. Matthiesen, S. Fält, A. Badolato, M. Atatüre, Phys. Rev. B **81**, 035332 (2010)
101. F. Maier, D. Loss, Phys. Rev. B **85**, 195323 (2012)
102. H. Ribeiro, F. Maier, D. Loss, Phys. Rev. B **92**, 075421 (2015)
103. D. Heiss, S. Schaeck, H. Huebl, M. Bichler, G. Abstreiter, J.J. Finley, D.V. Bulaev, D. Loss, Phys. Rev. B **76**, 241306 (2007)
104. Y. Li, N. Sinitsyn, D.L. Smith, D. Reuter, A.D. Wieck, D.R. Yakovlev, M. Bayer, S.A. Crooker, Phys. Rev. Lett. **108**, 186603 (2012)
105. R. Dahbashi, J. Hübner, F. Berski, K. Pierz, M. Oestreich, Phys. Rev. Lett. **112**, 156601 (2014)
106. D. Brunner, B.D. Gerardot, P.A. Dalgarno, G. Wüst, K. Karrai, N.G. Stoltz, P.M. Petroff, R.J. Warburton, Science **325**, 70 (2009)
107. K. De Greve, P.L. McMahon, D. Press, T.D. Ladd, D. Bisping, C. Schneider, M. Kamp, L. Worschech, S. Hoefling, A. Forchel, Y. Yamamoto, Nat. Phys. **7**, 872 (2011)
108. A. Greilich, S.G. Carter, D. Kim, A.S. Bracker, D. Gammon, Nat. Photonics **5**, 703 (2011)
109. T.M. Godden, J.H. Quilter, A.J. Ramsay, Y. Wu, P. Brereton, S.J. Boyle, I.J. Luxmoore, J. Puebla-Nunez, A.M. Fox, M.S. Skolnick, Phys. Rev. Lett. **108**, 017402 (2012)
110. S. Varwig, A. René, A. Greilich, D.R. Yakovlev, D. Reuter, A.D. Wieck, M. Bayer, Phys. Rev. B **87**, 115307 (2013)
111. P. Fallahi, S.T. Yilmaz, A. Imamoglu, Phys. Rev. Lett. **105**, 257402 (2010)
112. E.A. Chekhovich, A.B. Krysa, M.S. Skolnick, A.I. Tartakovskii, Phys. Rev. Lett. **106**, 027402 (2011)
113. H. Kurtze, D.R. Yakovlev, D. Reuter, A.D. Wieck, M. Bayer, Phys. Rev. B **85**, 195303 (2012)
114. E.A. Chekhovich, M.M. Glazov, A.B. Krysa, M. Hopkinson, P. Senellart, A. Lemaître, M.S. Skolnick, A.I. Tartakovskii, Nat. Phys. **9**, 74 (2013)
115. A.J. Bennett, M.A. Pooley, Y. Cao, N. Sköld, I. Farrer, D.A. Ritchie, A.J. Shields, Nat. Commun. **4**, 1522 (2013)
116. J. Houel, J.H. Prechtel, A.V. Kuhlmann, D. Brunner, C.E. Kuklewicz, B.D. Gerardot, N.G. Stoltz, P.M. Petroff, R.J. Warburton, Phys. Rev. Lett. **112**, 107401 (2014)
117. J.H. Prechtel, F. Maier, J. Houel, A.V. Kuhlmann, A. Ludwig, A.D. Wieck, D. Loss, R.J. Warburton, Phys. Rev. B **91**, 165304 (2015)
118. M. Fleischhauer, A. Imamoglu, J.P. Marangos, Rev. Mod. Phys. **77**, 633 (2005)
119. J. Hansom, C.H.H. Schulte, C. Le Gall, C. Matthiesen, E. Clarke, M. Hugues, J.M. Taylor, M. Atatüre, Nat. Phys. **10**, 725 (2014)
120. A.V. Kuhlmann, J. Houel, D. Brunner, A. Ludwig, D. Reuter, A.D. Wieck, R.J. Warburton, Rev. Sci. Instrum. **84**, 073905 (2013)

121. C. Latta, A. Hoegele, Y. Zhao, A.N. Vamivakas, P. Maletinsky, M. Kroner, J. Dreiser, I. Carusotto, A. Badolato, D. Schuh, W. Wegscheider, M. Atatüre, A. Imamoglu, Nat. Phys. **5**, 758 (2009)
122. A. Högele, M. Kroner, C. Latta, M. Claassen, I. Carusotto, C. Bulutay, A. Imamoglu, Phys. Rev. Lett. **108**, 197403 (2012)
123. D. Press, T.D. Ladd, B. Zhang, Y. Yamamoto, Nature **456**, 218 (2008)